Lattice dynamics and mixing of polar phonons in the rare-earth orthoferrite $TbFeO_3$

R. M. Dubrovin,[1,*] E. M. Roginskii,[1] V. A. Chernyshev,[2] N. N. Novikova,[3] M. A. Elistratova,[1] I. A. Eliseyev,[1] A. N. Smirnov,[1] A. I. Brulev,[1,4] K. N. Boldyrev,[3] V. Yu. Davydov,[1] R. V. Mikhaylovskiy,[5] A. M. Kalashnikova,[1] and R. V. Pisarev[1]

[1] *Ioffe Institute, Russian Academy of Sciences, 194021 St. Petersburg, Russia*
[2] *Department of Basic and Applied Physics, Ural Federal University, 620002 Yekaterinburg, Russia*
[3] *Institute of Spectroscopy, Russian Academy of Sciences, 108840 Moscow, Troitsk, Russia*
[4] *University of Nizhny Novgorod, 603022 Nizhny Novgorod, Russia*
[5] *Department of Physics, Lancaster University, Bailrigg, Lancaster LA1 4YW, United Kingdom*

(Dated: September 4, 2024)

Rare-earth orthoferrites are a promising platform for antiferromagnetic spintronics with a rich variety of terahertz spin and lattice dynamics phenomena. For instance, it has been experimentally demonstrated that the light-driven optical phonons can coherently manipulate macroscopic magnetic states via nonlinear magnetophononic effects. Here using $TbFeO_3$ as an example, we reveal the origin of the mode mixing between the LO and TO phonons, which is important for understanding of nonlinear phononics. We performed a comprehensive study of the lattice dynamics of $TbFeO_3$ single crystal by polarized infrared and Raman scattering spectroscopic techniques, experimentally obtained and carefully analyzed the spectra of anisotropic complex dielectric functions in the far-infrared spectral range. This allowed us to reliably identify the symmetries and parameters of most infrared- and Raman-active phonons. Next, the experimental studies were supplemented by the lattice dynamics calculations which allowed us to propose the normal mode assignments. We reveal that the relation between LO and TO polar phonons is complex and does not strictly follow the "LO-TO rule" due to the strong mode mixing. We further analyze how displacements of different ions contribute to phonon modes and reveal that magnetic Fe ions are not involved in Raman-active phonons, thus shedding a light on a lack of spin phonon coupling for such phonons. The obtained results establish a solid basis for further in-depth experimental research in the field of the nonlinear phononics and magnetophononics in rare-earth orthoferrites.

I. INTRODUCTION

Rare-earth orthoferrites $RFeO_3$, where R stands for a rare-earth cation, are a universe for researchers in the area of spin physics because of the many exciting magnetic [1–14], magnetoelectric [15–20], multiferroic [21] and other properties observed in them. The orthoferrites $RFeO_3$ have been known for over 60 years and in many ways have already become well characterized model materials, but nevertheless their potential has not been fully realised and they are still a universal playground for the modern magnetism [22]. The presence of the $3d$ Fe^{3+} and $4f$ R^{3+} magnetic cations in different sublattices leads to competition between $Fe-Fe$, $R-Fe$, and $R-R$ exchange interactions and, in turn, to a complex magnetic phase diagram with a variety of spin-reorientation transitions [23]. Thus, the control of macroscopic magnetic states in rare-earth orthoferrites creates a rich platform for application in high speed data storage devices [1; 3; 24–30].

It is known that the lattice dynamics is responsible for important physical properties of crystals such as thermodynamical characteristics, superconductivity, phase transitions [31]. Moreover, nowadays the resonant driving of phonons in crystals is a unique route for coherent manipulation of the lattice and its associated functional properties at high rate, which is not available in equilibrium [32]. Meanwhile, orthoferrites are archetypical magneto-phononic materials in which it has been experimentally shown for the first time that resonant excitation of polar phonons using intense infrared light provides a unique opportunity for coherent control of macroscopic magnetic states [4; 7; 33]. The lattice dynamics of orthoferrites $RFeO_3$ in the center of the Brillouin zone have been studied in depth by numerical simulations [33–37] and Raman spectroscopy [35; 38–51]. In contrast, the infrared-active phonons in orthoferrites $RFeO_3$ have been studied in most cases in non-single crystal samples [52–58] and the studies carried out on single crystal samples did not concern polarizations along the main crystallographic axes [7; 59; 60], which makes it almost impossible to establish the symmetry of the studied polar phonons using the selection rules for polarization of radiation. To our knowledge, there is only one recent paper with results of the polarization-resolved measurements on the orthoferrite single crystal [61].

In this paper, we present results of systematic study of the lattice dynamics of orthoferrite $TbFeO_3$ high quality single crystals employing complementary infrared reflectivity and Raman scattering polarized spectroscopic techniques supported by corresponding ab initio calculations. The anisotropic complex dielectric function was accurately extracted from spectroscopic reflectivity measurements at infrared frequencies for the main crystallographic axes of the studied orthoferrite. A rigorous

* dubrovin@mail.ioffe.ru

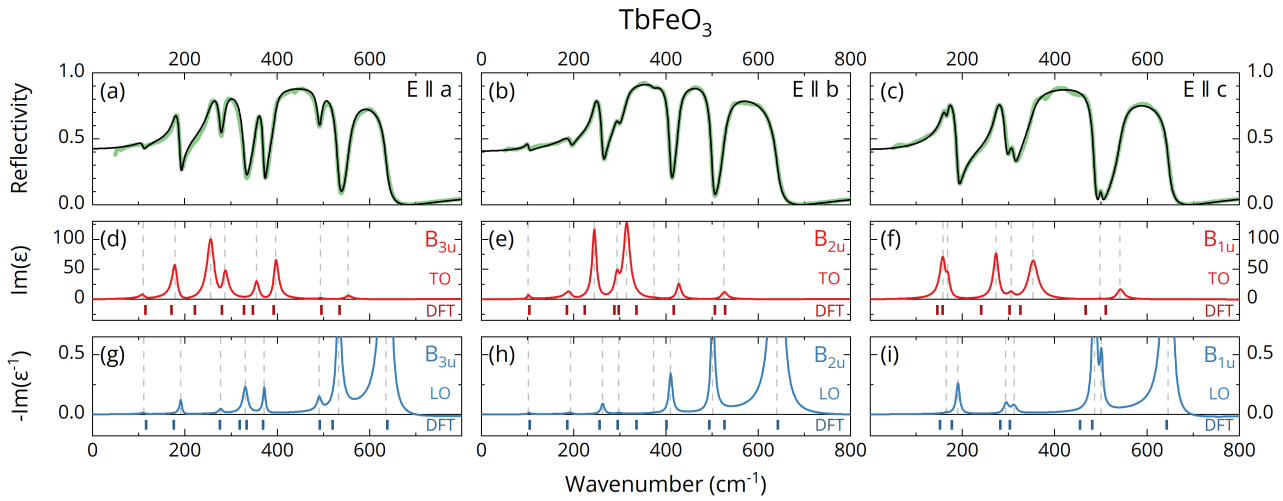

FIG. 1. The polarized infrared reflectivity spectra at ambient conditions with the electric field of light **E** polarized along the (a) a, (b) b, and (c) c axes of the orthoferrite $TbFeO_3$. The solid black lines are fits based on the generalized oscillator model of the complex dielectric permittivity $\varepsilon(\omega) = \varepsilon_1(\omega) - i\varepsilon_2(\omega)$ according to Eq. (S1) in SM [62].Spectra of the imaginary part of the complex dielectric permittivity $\Im[\varepsilon(\omega)]$ and the inverse complex dielectric permittivity $-\Im[\varepsilon^{-1}(\omega)]$ obtained from the fit of the reflectivity spectra corresponding of the TO and LO polar phonons with the symmetries (d), (g) B_{3u}, (e), (h) B_{2u}, and (f), (i) B_{1u}, respectively. Red and blue sticks present the calculated TO and LO frequencies of the polar phonons, respectively.

examination of obtained experimental spectra allowed us to successfully identify frequencies and symmetries of most of the infrared- and Raman-active phonons. Moreover, the analysis of the calculated eigendisplacements allowed us to establish the couplings between LO and TO phonons which sets the grounds for further exploiting of phononics in this class of crystals. Note that our research is focused on the room temperature because all rare-earth orthoferrites except $SmFeO_3$ have the same Γ_4 magnetic configuration at ambient conditions [3] which is important for application in nonlinear phononics and the conclusions of the paper can be extended to all these orthoferrites.

This paper is organized as follows. The samples of $TbFeO_3$ and an outline of the experimental setups and computational details for studying the lattice dynamics are introduced in the Supplemental Material (SM) [62]. Section II presents and discusses the experimental data on infrared and Raman spectroscopy, supported by first principles calculations, which allow us to reveal the strong LO-TO mixing and follow the phonon genesis. Concluding Remarks are given in Sec. III.

II. RESULTS AND DISCUSSION

Rare-earth orthoferrite $TbFeO_3$ has the orthorhombic crystal structure with the space group $Pbnm$ [#62, D_{2h}^{16}, $Pnma$ with nonconventional coordinate axes orientation, $Pnma(a,b,c) \Leftrightarrow Pbnm(b,c,a)$] and four formula units per unit cell $Z = 4$ [89; 90]. The lattice parameters measured by the x-ray diffraction at room temperature are $a = 5.33$ Å, $b = 5.6$ Å, and $c = 7.65$ Å which are close to the literature data [18]. The unit cell contains 20 ions occupying the Wyckoff positions $4c$ for Tb^{3+}, $4b$ for Fe^{3+}, $4c$ and $8d$ for O^{2-}. This orthorhombic structure of $TbFeO_3$ originates from the distortion of the ideal cubic perovskite structure with space group $Pm\overline{3}m$ caused by the ionic size mismatch [91].

The group-theoretical analysis of $Pbnm$ orthoferrites $RFeO_3$ predicts 60 phonons at the center of the Brillouin zone [86]:

$$\Gamma_{\text{total}} = \underbrace{B_{1u} \oplus B_{2u} \oplus B_{3u}}_{\Gamma_{\text{acoustic}}} \oplus \underbrace{7A_g \oplus 7B_{1g} \oplus 5B_{2g} \oplus 5B_{3g}}_{\Gamma_{\text{Raman}}} \oplus \underbrace{7B_{1u} \oplus 9B_{2u} \oplus 9B_{3u}}_{\Gamma_{\text{IR}}} \oplus \underbrace{8A_u}_{\Gamma_{\text{silent}}}, \quad (1)$$

among which there are 3 acoustic, 24 Raman-active, 25 infrared-active (polar) and 8 silent non-degenerate modes. We note that silent modes active neither in Raman nor in infrared spectra can be observed in Hyper-Raman experiments. Table I lists the characters for all modes.

A comprehensive description of $TbFeO_3$ single crystal samples and an outline of the experimental setups and computational details for studying the lattice dynamics and features of its analysis are given in the Supplemental Material [62].

A. Infrared spectroscopy

The reflectivity spectra of the orthoferrite $TbFeO_3$ measured at ambient conditions for the polarization of

TABLE I. Character table of irreducible representations of the $D_{2h}(mmm)$ point group in the $Pbnm$ coordinate axes orientation.

D_{2h}	E	$C_2(x)$	$C_2(y)$	$C_2(z)$	i	$\sigma(xy)$	$\sigma(yz)$	$\sigma(xz)$	functions
A_g	+1	+1	+1	+1	+1	+1	+1	+1	x^2, y^2, z^2
B_{1g}	+1	−1	−1	+1	+1	+1	−1	−1	R_z, xy
B_{2g}	+1	−1	+1	−1	+1	−1	−1	+1	R_y, xz
B_{3g}	+1	+1	−1	−1	+1	−1	+1	−1	R_x, yz
A_u	+1	+1	+1	+1	−1	−1	−1	−1	xyz
B_{1u}	+1	−1	−1	+1	−1	−1	+1	+1	z, x^2z, y^2z, z^3
B_{2u}	+1	−1	+1	−1	−1	+1	+1	−1	y, yx^2, y^3, yz^2
B_{3u}	+1	+1	−1	−1	−1	+1	−1	+1	x, x^3, xz^2, xy^2

TABLE II. Experimental frequencies ω (cm^{-1}), dampings γ (cm^{-1}), and dielectric strengths $\Delta\varepsilon$ of the TO and LO polar phonons in $TbFeO_3$ at room temperature in comparison with the results of DFT calculations presented in parentheses.

Sym.	ω_{TO}		γ_{TO}	ω_{LO}		γ_{LO}		$\Delta\varepsilon$
	109.7	(112.4)	12.5	111	(112.8)	11	0.64	(0.31)
	179.1	(166.7)	13.6	191.2	(175.6)	6.4	4.17	(4.83)
	256.2	(230.3)	19.2	277.5	(266.9)	9.3	7.51	(12.83)
	286.6	(274.7)	14	330.8	(314.1)	12.3	2.17	(1.48)
B_{3u}	—	(322.5)	—	—	(323)	—	—	(0.02)
	355.6	(341.4)	12.5	372	(361.1)	6.54	1.03	(1.26)
	396.8	(390.7)	12.3	490.8	(490.9)	11.3	2.05	(2.41)
	493.4	(495)	11.5	532.9	(507.3)	12.4	0.04	(0.04)
	553.7	(521.5)	17.2	635.7	(610.8)	11.3	0.19	(0.22)
	101.3	(101.3)	7.4	102.3	(101.8)	8	0.46	(0.28)
	191.2	(182.3)	17.3	193.8	(182.4)	14.1	0.91	(0.005)
	245	(226.2)	11	262.8	(249.8)	8.7	5.18	(9.44)
	294	(286.5)	11.9	297.5	(287.5)	11.9	1.38	(1.21)
B_{2u}	314.8	(294.6)	16.8	410.2	(396.3)	9.2	6.74	(8.54)
	374	(329.6)	15	373.6	(329.6)	14.8	0.03	(-0.0002)
	427.5	(416.8)	11.6	501.3	(480.4)	9.28	0.69	(0.96)
	—	(491.8)	—	—	(513.3)	—	—	(0.25)
	526	(514.4)	16.1	640.9	(614.6)	14.6	0.37	(0.03)
	158.7	(149.4)	15.2	166	(153.1)	8.7	6.43	(6.64)
	168.7	(155.7)	8.3	190.8	(174.3)	9	1.53	(3.2)
	273.6	(243.7)	13.5	294.4	(284.6)	12.1	3.73	(8.33)
B_{1u}	306.1	(297.2)	16.1	312.6	(297.3)	13.2	0.49	(0.003)
	353.4	(332.2)	24.6	486.5	(442.4)	8.1	4.52	(5.23)
	498.2	(459.3)	7.7	501.3	(472.8)	7.8	0.02	(0.22)
	542	(491.4)	18.1	645.6	(600.3)	10.6	0.56	(0.51)

the electric field of light $\mathbf{E}$ parallel to the a, b and c axes are shown by the green lines in Figs. 1(a)–1(c). According to the group-theoretical analysis [86], polar phonons with B_{3u}, B_{2u}, and B_{1u} symmetries are active for electric field polarizations along the a, b, and c axes, respectively. The reflection bands observed in the spectra allow us to readily identify 7 out of 7 B_{1u}, 8 out of 9 B_{2u}, and 8 out of 9 B_{3u} polar phonons symmetry-allowed for corresponding polarization.

There is a fair agreement between experimental spectra (green lines) and fits obtained using Eqs. (S1) and (S2) in SM [62] (black lines) seen for all studied polarizations in Figs. 1(a)–1(c). The spectra of the $\Im[\varepsilon(\omega)]$ and $\Im[\varepsilon^{-1}(\omega)]$ corresponding to the fits are shown by red and blue lines in Figs. 1(d)–1(f) and 1(g)–1(i), respectively. The frequencies and dampings of polar phonons for studied orthoferrite $TbFeO_3$ derived from the fits of the reflectivity spectra are listed in Table II. It is worth noting that there is the generalized Lowndes condition $\sum_j(\gamma_{jLO}-\gamma_{jTO})>0$ that must be satisfied to keep positive $\Im[\varepsilon(\omega)]$ for insulator crystals [81; 92; 93]. As follows from Table II, this condition is somewhat violated in our case of the best fits, but nevertheless no significant value of $\Im[\varepsilon(\omega)]<0$ is observed as can be seen in Figs. 1(d)–1(i).

TABLE III. Experimental lattice parameters a, b and c (Å) obtained by the x-ray diffraction, values of the static ε_0 and high frequency ε_∞ anisotropic dielectric permittivities in $TbFeO_3$ at room temperature in comparison with the results of DFT calculations.

	Exp	DFT
a	5.33	5.49
b	5.6	5.81
c	7.65	7.92
ε_0^a	21.7	29.2
ε_0^b	20.5	30.1
ε_0^c	22.6	26.4
ε_∞^a	4.81	5.83
ε_∞^b	4.82	5.97
ε_∞^c	4.79	5.70

The contribution from each jth polar phonon of a specific symmetry to the anisotropic static dielectric permittivity $\varepsilon_0=\varepsilon_\infty+\sum_j\Delta\varepsilon_j$ is determined by its dielectric strength [94]

$$\Delta\varepsilon_j=\frac{\varepsilon_\infty}{\omega_{jTO}^2}\frac{\prod_k\omega_{kLO}^2-\omega_{jTO}^2}{\prod_{k\neq j}\omega_{kTO}^2-\omega_{jTO}^2}. \quad (2)$$

The TO and LO frequencies of polar phonons from the fits were used to obtain the values of dielectric strengths $\Delta\varepsilon$ by using Eq. (2) which are listed in Table II. The values of the anisotropic static ε_0 and high frequency ε_∞ dielectric permittivities obtained from the reflectivity fit using Eq. (S1) in SM [62] are listed in Table III. This value of static dielectric permittivity ε_0 for $TbFeO_3$ is in fair agreement with data reported in literature for several

orthoferrites [95; 96].

It should be noted that the analysis of the experimental results using Eq. (S1) in SM [62] does not allow one to associate a given LO frequency with a TO frequency of the polar phonon with a specific symmetry. Moreover, Eq. (2) gives the same result for any relation between TO and LO frequencies of the polar phonons. However, there is the so-called "TO-LO rule" stating that for the each main crystallographic axis, the sequence of polar phonons is such that a TO frequency is always followed exactly by the corresponding LO frequency with an ascending frequency $\omega_{\mathrm{LO}} > \omega_{\mathrm{TO}}$, and LO-TO splitting is positive [97]. Thus, applying this rule, the LO frequency can be assigned to the TO frequency of the polar phonon with a specific symmetry, which gives reliable results for many crystals. Besides, often the LO and TO frequencies are grouped according to similarity in strength and width of the peaks in spectra of $\Im[\varepsilon(\omega)]$ and $\Im[\varepsilon^{-1}(\omega)]$ [98]. However, none of these empirical rules are canonical in general and the lattice dynamical calculations are an efficient way to identify LO-TO phonon pairs based on solid physical arguments.

B. Raman spectroscopy

The lattice dynamics at the Brillouin zone center in crystals is studied further by analysis of optical phonons which are active in Raman scattering. The experimental Raman spectra of the rare-earth orthoferrite $TbFeO_3$ in different polarizations measured at ambient conditions are presented in Fig. 2. The difference of the values of the diagonal elements of the Raman tensor (S3) in SM [62] leads to unequal intensities of the fully symmetric A_g phonons for various parallel polarizations. The obtained Raman spectra have been carefully analysed, and 7 out of 7 expected A_g phonons, 6 out of 7 for B_{1g}, 4 out of 5 for B_{2g}, and 5 out of 5 for B_{3g} modes were reliably identified as shown by dashed lines in Fig. 2. The frequencies, intensities and full widths at half maximum (FWHM) of the identified phonons were extracted by fitting of the obtained Raman spectra by a sum of Voigt profiles [99] and listed in Table IV. Small leaks of phonons in forbidden polarizations were observed due to almost unavoidable depolarization effect in the optical elements and slight misalignment of the polarization of light with respect to the crystal axes. It is worth noting that the intensities of the A_g modes are significantly higher than for the B_g phonons, as shown in Fig. 2. The calculated frequencies of the Raman-active phonons in rare-earth orthoferrite $TbFeO_3$ are in fair agreement with experimental as listed in Table IV. Besides, there is a fair agreement between the phonon frequencies obtained in our experiment and the ones from Refs. [39; 41], as can be seen in Table IV.

To reveal the symmetry of the weak and overlapping lines we performed angle-resolved Raman measurements for both parallel ($\boldsymbol{e}_i \parallel \boldsymbol{e}_s$) and crossed ($\boldsymbol{e}_i \perp \boldsymbol{e}_s$) polarizations. The experimental angular-dependent spectral intensity maps are shown in Fig. S1 in SM [62].As expected, the phonon lines exhibit strong anisotropy of Raman scattering. Note that the experimental intensity maps are in a fair agreement with results of the corresponding DFT calculations as can be seen in Figs. S1 and S2 in SM [62].

Further, the experimental angular dependences of phonon intensity were extracted (see colored open circles in Fig. S3 in SM [62]. To verify the phonon symmetry, the obtained angular dependences were fitted using Eqs. (S4) and (S3) as shown by colored solid lines in Fig. S3 in SM [62]. It should be noted that 3 parallel and 3 crossed angular dependences are fitted at once using a single Raman tensor. A satisfactory agreement between the experimental data and fit lines is observed as seen in Fig. S3 in SM [62]. A_g modes have the highest intensity along the main crystal axes in the parallel configuration and at 45° to them in the crossed one. For B_g modes, in contrast, the highest intensity is along the main crystal axes in the crossed geometry and at 45° in the parallel one. Thus, this approach allowed us to reliably determine the symmetry of the Raman-active phonons with

TABLE IV. Frequencies (cm^{-1}) and full widths at half maximum (FWHM, cm^{-1}) of the Raman-active A_g, B_{1g}, B_{2g}, and B_{3g} phonons for $TbFeO_3$ at ambient conditions in comparison with results of DFT calculations and the experimental data from Refs. [39; 41].

	Experiment		DFT		Experiment	
Sym.	Freq.	FWHM	Freq.[a]	Freq.[b]	Freq.[c]	Freq.[d]
A_g	111	3.3	108.1	111.8	112.5	109
	139.7	6.5	130.5	131.8	143.9	140
	257.9	14	253.2	253.1	261.9	273
	331.6	7.4	319.2	330	334.5	329
	407.8	9.9	388.1	402.4	410.9	—
	415.4	25.3	404.5	408.8	420.1	406
	487.2	10.8	471.6	487.6	490.1	480
B_{1g}	109.8	5.6	106.5	109.6	107.7	—
	159.1	6.8	155.6	157.8	160.1	139
	296.6	14	297.2	293.9	302.7	—
	359	9.9	338.8	351.7	—	329
	483.6	9.4	464.6	483.1	485.6	479
	—	—	520.1	529.3	535.8	—
	639.6	—	608.3	641.1	—	—
B_{2g}	128.1	6.2	118.2	122.6	—	—
	321.5	12.2	297.8	314.3	—	—
	428.1	20.2	382.1	412.4	433.3	418
	466.8	—	446.9	463.7	468.8	—
	—	—	629.8	667.8	—	—
B_{3g}	149.1	5.2	132.8	140.9	—	159
	252.4	17.7	235.6	239.8	251.9	249
	356.2	10.8	339.8	347.8	359.2	354
	426	20.7	393.2	409.6	427.7	426
	629.3	69.1	581.8	622.8	—	—

[a] VASP
[b] CRYSTAL14
[c] Ref. [41].
[d] Ref. [39].

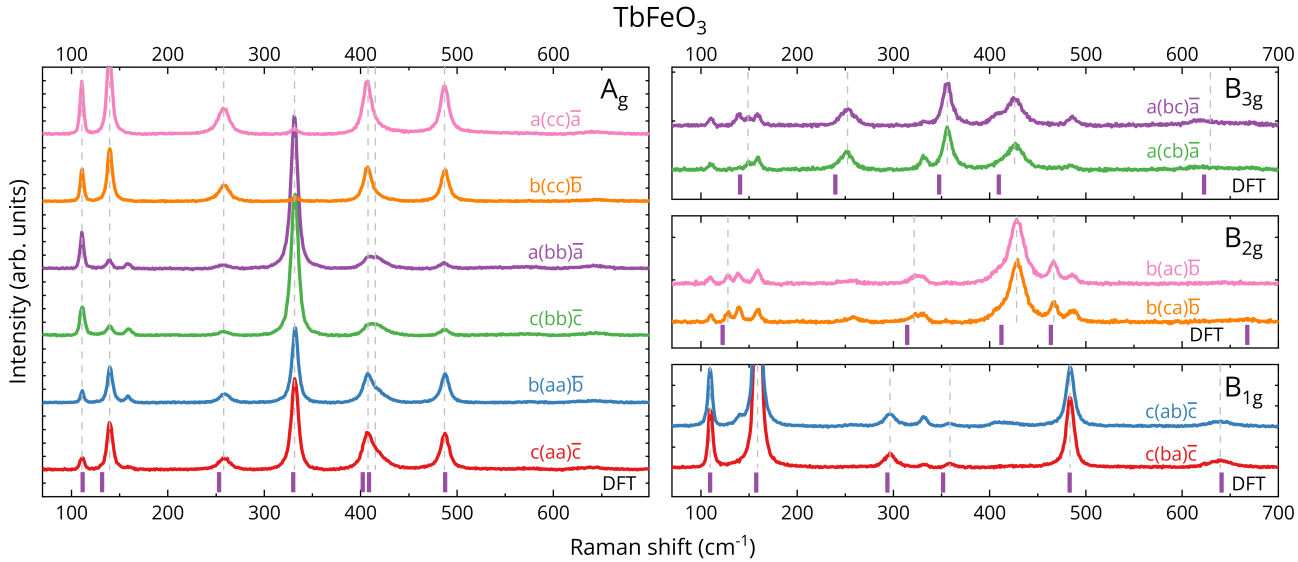

FIG. 2. Polarized Raman spectra of the A_g, B_{3g}, B_{2g}, and B_{1g} phonons at ambient conditions for orthoferrites $TbFeO_3$, respectively. The polarization configuration are given in Porto's notation as described in the text. Purple sticks in the bottom of each plot present the calculated phonon frequencies.

weak corresponding spectral lines. Figure S4 shows angular dependences of phonon intensity derived from DFT calculations and a fair agreement with the experiment can be observed (see Fig. S3 in SM [62]).

Along with polarized Raman spectra [see Figs. 3(a)-3(c)], we also have calculated the joint density of vibrational states (JDOS) projected onto ionic contributions for the Raman-active phonons. Figs. 3(e)-3(h) show that Tb and O ions are equally involved in the vibrations corresponding to the low-frequency modes. With increasing frequency, due to the large mass of the rare-earth atoms, the role of Tb ions in the phonon displacements uniformly decreases and for the oscillation above $480\,\mathrm{cm}^{-1}$ take almost no part. It should be noted that according to the calculations, the Fe ions remain fixed for all Raman-active phonons. This is due to the fact that, based on symmetry considerations, the Tb ($4c$) and O ($4c$ and $8d$) ions are active for the both *gerade* and *ungerade* $A_g \oplus B_{1g} \oplus B_{2g} \oplus B_{3g} \oplus A_u \oplus B_{1u} \oplus B_{2u} \oplus B_{3u}$ modes while Fe ($4b$) ions are active only for *ungerade* $A_u \oplus B_{1u} \oplus B_{2u} \oplus B_{3u}$ modes [86]. It follows that for Raman-active modes the involvement of Fe ions is forbidden by symmetry and they can only contribute to polar phonons as shown in Fig. 4. Apparently, the absence of spin-phonon coupling for Raman-active modes at the magnetic ordering of Fe ions observed in rare-earth orthoferrites is related to this fact [49].

C. Lattice dynamics calculations

The common approach of lattice dynamics study within DFT is based on calculations of the dynamical matrix D followed by solving the general eigenvalue problem [100]. Taking into account only short-range interaction [analytical (A) contribution] to the dynamical matrix $D_{ij}^{\alpha\beta} = D_{ij}^{\mathrm{A},\alpha\beta}$ at the Γ point of the Brillouin zone, where α and β are the direction indices, i and j are atomic indices, the solution of the eigenstate equation $D|\xi_m^{\mathrm{TO}}\rangle = \omega_{\mathrm{TO},m}^2|\xi_m^{\mathrm{TO}}\rangle$ gives eigenvector ξ_m^{TO} and frequency $\omega_{\mathrm{TO},m}$ of the mth TO phonon. To account for the long-range macroscopic electric field which is induced by collective atomic displacements, the non-analytical (NA) contribution to the dynamical matrix $D_{ij}^{\alpha\beta} = D_{ij}^{\mathrm{A},\alpha\beta} + D_{ij}^{\mathrm{NA},\alpha\beta}$ is necessary, which in the vicinity of the Γ point takes the form [100; 101]

$$D_{ij}^{\mathrm{NA},\alpha\beta} = \frac{1}{\sqrt{M_i M_j}} \frac{4\pi e^2}{\Omega} \frac{[\mathbf{q}\cdot\mathbf{Z}_i]_\alpha [\mathbf{q}\cdot\mathbf{Z}_j]_\beta}{\mathbf{q}\cdot\boldsymbol{\varepsilon}_\infty\cdot\mathbf{q}}\bigg|_{\mathbf{q}\to 0}, \quad (3)$$

where M_i is the mass of the ith ion, e is the elementary charge, Ω is the volume of the unit cell, $\mathbf{Z}_i$ is the Born effective charge tensor, $\mathbf{q}$ is the wave vector, and $\boldsymbol{\varepsilon}_\infty$ is the high-frequency dielectric permittivity tensor. Then the eigenvector ξ_m^{LO} and frequency $\omega_{\mathrm{LO},m}$ of the mth LO phonon can be obtained by solving the equation $D|\xi_m^{\mathrm{LO}}\rangle = \omega_{\mathrm{LO},m}^2|\xi_m^{\mathrm{LO}}\rangle$. It is worth noting that the calculations of the TO and LO modes involve the diagonalization of different dynamical matrices $D = D^{\mathrm{A}}$ and $D = D^{\mathrm{A}} + D^{\mathrm{NA}}$, respectively. Thus, in general the eigenvectors ξ^{LO} and ξ^{TO} for polar phonons are not necessarily equal. Moreover, the NA term $D_{ij}^{\mathrm{NA},\alpha\beta}$ is non-diagonal and often causes a strong mixing of different modes caused by the Coulomb interaction, i.e. several TO modes may contribute to a single LO mode [98; 102]. Note that the NA contribution affects only polar phonons, whereas the frequencies and eigenvectors of non-polar phonons remain unchanged in the vicinity of the Γ point.

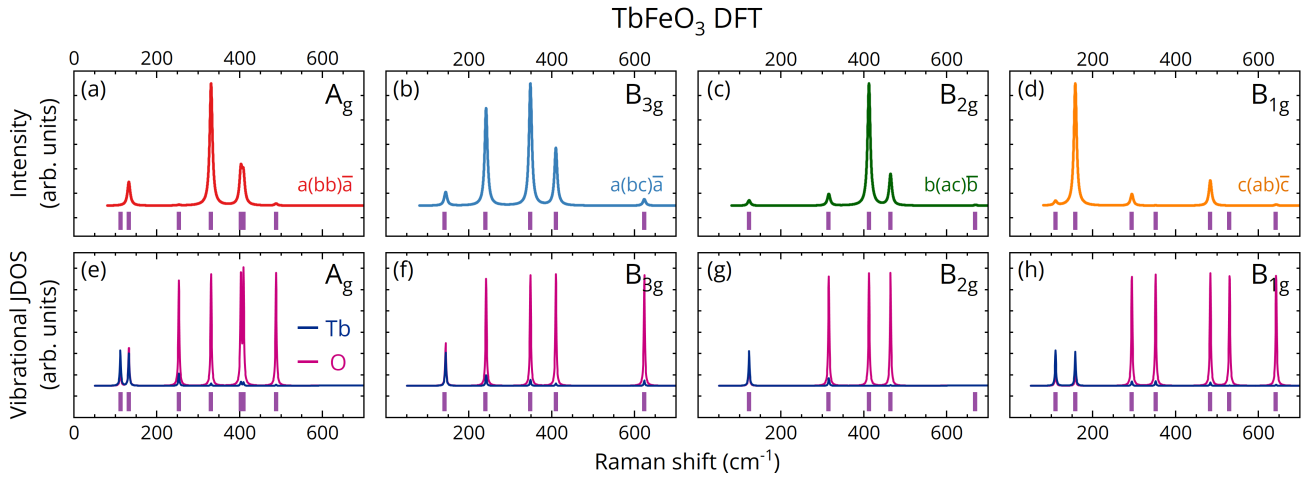

FIG. 3. Calculated polarized Raman spectra and joint density of vibrational states (JDOS) projected onto ionic contributions of (a,e) A_g, (b,f) B_{3g}, (c,g) B_{2g}, and (d,h) B_{1g} phonons for $TbFeO_3$, respectively. The polarization configuration are given in Porto's notation as described in the text. Purple sticks in the bottom of each plot present the calculated phonon frequencies.

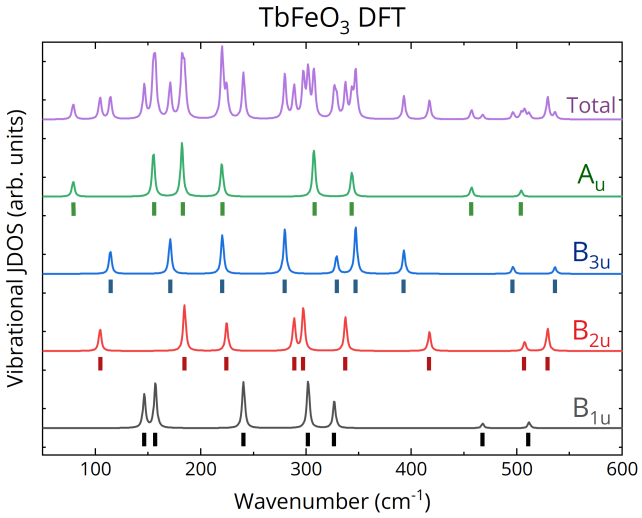

FIG. 4. Calculated joint density of vibrational states (JDOS) of the Fe ions projected onto the polar A_u, B_{1u}, B_{2u}, B_{3u} modes and the total phonon spectrum for $TbFeO_3$. Color sticks in the bottom of each plot present the calculated phonon frequencies.

It is well known that each normal (TO) mode corresponds to a single irreducible representation of the point group of the crystal, whereas all other possible modes can be represented as linear combinations of these irreducible representations [31]. That is, the eigenvectors of normal modes satisfy the orthonormal conditions $\langle \xi_m^{\rm TO} | \xi_n^{\rm TO} \rangle = \delta_{mn}$, where δ_{mn} is the Kronecker delta, and form a basis. Thus, it is reasonable to expand the eigenvector of the mth LO mode to a linear combination of the normal modes

$$|\xi_m^{\rm LO}\rangle = \sum_n C_{mn} |\xi_n^{\rm TO}\rangle. \quad (4)$$

Note that non-zero expansion coefficients $C_{mn} \neq 0$ can give only polar modes with the same polarization (basis function). The contribution from the acoustic mode is usually negligible, so only the polar TO modes are taken into account in the decomposition from Eq. (4). Thereby, it is useful to analyze the overlap matrix which represents the degree of correlation between the $m^{\rm th}$ LO and $n^{\rm th}$ TO eigenvectors of polar phonons with a specific symmetry according to the expression [101; 103]

$$C_{mn} = \langle \xi_m^{\rm LO} | \xi_n^{\rm TO} \rangle, \quad (5)$$

where $\langle \ldots \rangle$ denotes scalar product. When the "TO-LO rule" is strictly satisfied for all polar phonons, the C matrix takes a form in which the elements on the main diagonal are many fold larger than the others. For ideal crystals where eigenvectors for TO and LO modes are equal $|\xi^{\rm TO}\rangle = |\xi^{\rm LO}\rangle$ the overlap matrix C is the identity matrix with ones on the main diagonal and zeros elsewhere. In real crystals, mode mixing caused by Coulomb interaction is expressed in the form that for some LO modes the relevant elements of the overlap matrix C are essentially non-zero for several TO modes [101; 104; 105].

To gain insight into the phonon landscape of the orthoferrite $TbFeO_3$, we performed the first principles calculations of the lattice dynamics in the vicinity of the Γ point of the Brillouin zone. The calculated lattice parameters a, b, and c, static ε_0 and high frequency ε_∞ anisotropic dielectric permittivities in comparison to experimental values are listed in Table III. The Born effective charge tensors $\mathbf{Z}$ of ions in $TbFeO_3$ are listed in Table V. The LO modes were obtained with the NA term [Eq. (3)] taken into account in the calculations. The computed frequencies $\omega_{\rm TO}$ and $\omega_{\rm LO}$ and dielectric strengths $\Delta\varepsilon$ of the polar phonons are listed in parentheses in Table II. It is worth noting that there is a fair agreement between the calculation and experimental results. Moreover, the obtained frequencies of the Raman-active phonons are

TABLE V. Calculated Born effective charge tensors $\mathbf{Z}$ of the ions in $TbFeO_3$.

Tb (4c)	Fe (4b)	O (4c)	O (8d)
$\begin{pmatrix} 4.02 & 0.29 & 0 \\ 0.2 & 3.98 & 0 \\ 0 & 0 & 3.6 \end{pmatrix}$	$\begin{pmatrix} 4.02 & 0.39 & 0.48 \\ -0.19 & 4.25 & -0.12 \\ -0.32 & -0.2 & 4.03 \end{pmatrix}$	$\begin{pmatrix} -2.55 & -0.32 & 0 \\ -0.46 & -2.12 & 0 \\ 0 & 0 & -3.32 \end{pmatrix}$	$\begin{pmatrix} -2.75 & -0.53 & -0.08 \\ -0.57 & -3.05 & -0.17 \\ -0.04 & -0.2 & -2.16 \end{pmatrix}$

TABLE VI. Calculated frequencies $\omega_{\rm TO}$, $\omega_{\rm LO}$, $\tilde{\omega}_{\rm LO}$ (cm^{-1}) and oscillator strengths S (cm^{-2}) of the polar B_{3u}, B_{2u}, and B_{1u} phonons for $TbFeO_3$.

Sym.	$\omega_{\rm TO}$	$\omega_{\rm LO}$	$\tilde{\omega}_{\rm LO}$	S
	112.4	112.8	115.3	4.3 10^3
	166.7	175.6	225.3	1.4 10^5
	230.3	266.9	412.1	6.8 10^5
	274.7	314.1	307.6	1.1 10^5
B_{3u}	322.5	323	323.1	2.2 10^3
	341.4	361.1	376.5	1.5 10^5
	390.7	490.9	464.6	3.6 10^5
	495	507.3	496.8	1.1 10^4
	521.5	610.8	531.3	6.1 10^5
	101.3	101.8	103.7	3 10^3
	182.3	182.4	182.4	2 10^2
	226.2	249.8	368.6	5.1 10^5
	286.5	287.5	315.5	1.1 10^5
B_{2u}	294.6	396.3	465.6	7.7 10^5
	329.6	329.6	329.6	25
	416.8	480.4	450.4	1.7 10^5
	491.8	513.3	502.6	6.3 10^4
	514.4	614.6	515.6	7.7 10^3
	149.4	153.1	217.1	1.5 10^5
	155.7	174.3	192.9	6.4 10^4
	243.7	284.6	377.0	4.7 10^5
B_{1u}	297.2	297.3	297.3	3.5 10^2
	332.2	442.4	455.0	5.6 10^5
	459.3	472.8	467.6	4.3 10^3
	491.4	600.3	512.1	1.2 10^5

in good agreement with experimental data presented in Refs. [39; 41] as can be seen in Table IV.

To establish the relationship between the TO and LO modes, we calculated the overlap matrices C which represent the correlations between their eigenvectors using Eq. (5). The resulting overlap matrices C for B_{3u}, B_{2u}, and B_{1u} polar phonons are presented as a bar chart in Fig. 5. Here, the green background highlights the main diagonal of the overlap matrix C where the "TO-LO rule" should be satisfied. In other words, if this rule is met, the bar in the green background must be many times greater then those in the red background. Fig. 5 clearly shows that the "TO-LO rule" is strictly fulfilled only for a few LO modes with frequencies 113 cm^{-1}, 176 cm^{-1}, 323 cm^{-1} for B_{3u}, 102 cm^{-1}, 182 cm^{-1}, 288 cm^{-1} for B_{2u}, and 297 cm^{-1} for B_{1u}. For other LO modes (e.g. 491 cm^{-1}, 507 cm^{-1} for B_{3u}, and 480 cm^{-1} for B_{2u}) the relevant TO modes identified from the correlation analysis have a higher frequency so that $\omega_{\rm TO} > \omega_{\rm LO}$, thereby breaking the "TO-LO rule".

The highest frequency LO modes (611 cm^{-1} for B_{3u}, 615 cm^{-1} for B_{2u}, and 600 cm^{-1} for B_{1u},) largely correspond to the several lower-frequency TO modes due to the mixing described above as seen in Fig. 5. Perhaps this pronounced mixing manifests itself in the nonlinear magneto-phononic effects observed for the highest frequency LO modes in orthoferrites. Thus, the resonance mid-infrared pumping of these LO modes causes coherent spin and lattice dynamics at the frequencies of the quasi-antiferromagnetic resonance (25 cm^{-1}) and A_g modes (112 cm^{-1} and 162 cm^{-1}) in rare-earth orthoferrite $ErFeO_3$ [7; 33; 39]. The counter intuitive result here is that the direct excitation of LO modes by a transverse electromagnetic wave in bulk material should be forbidden because $\varepsilon_2(\omega_{\rm LO}) = 0$ assuming that $\gamma_{\rm LO} = 0$ [106]. Furthermore, the mechanism of nonlinear coupling between the high-frequency polar LO modes and Raman-active A_g modes was not disclosed in Ref. [7]. It is worth noting that the Raman-active A_g modes and polar phonons have the same symmetry away from the Γ point and thereby can directly interact with each other in the Brillouin zone, as discussed below. It is worth noting that LO modes in crystals have attracted special attention due to recently observed strongly enhanced light-matter interaction in the phononic epsilon-near-zero regime $\varepsilon_2(\omega_{\rm LO}) = 0$ which allows to switch the spin and polarization order parameters [107–109].

D. LO-TO mixing

To disclose how mixing of the polar TO phonons affects the LO modes and enables excitation of the latter by electromagnetic wave, we considered the effect of mode dynamical charges on the spectra of the complex dielectric permittivity $\varepsilon(\omega)$ in rare-earth orthoferrite $TbFeO_3$. Note that the highest frequency LO modes of different symmetries correspond to the major peaks in the spectra of the imaginary part of the inverse dielectric permittivity $-\Im[\varepsilon^{-1}(\omega)]$ as shown in Figs. 1(g)–1(i). Furthermore, these LO modes have the clear correlation with most TO phonons as can be seen in Fig. 5. Thus, it is convenient to analyze the relationship of the highest frequency LO modes of different symmetries with the TO modes of the same symmetry. For this, we consider the complex dielectric functions induced by some TO modes according

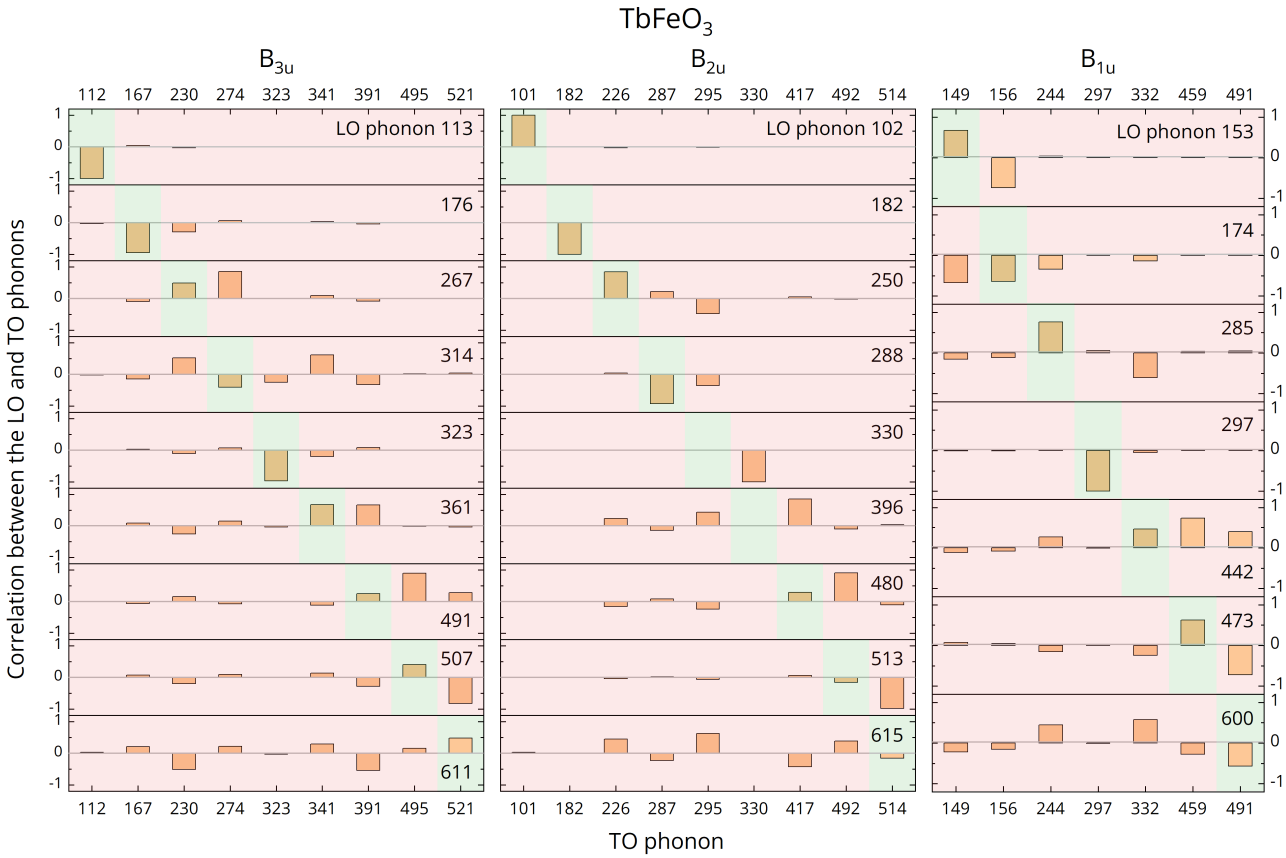

FIG. 5. The overlap matrices C which represent correlations between eigenvectors of LO and TO polar phonons with B_{3u} (left panel), B_{2u} (center panel), and B_{1u} (right panel) symmetry according to the DFT calculations at the Γ point of the Brillouin zone in $TbFeO_3$. The values of the LO phonon frequencies are given. The green background corresponds to the area where the "TO-LO rule" should be satisfied.

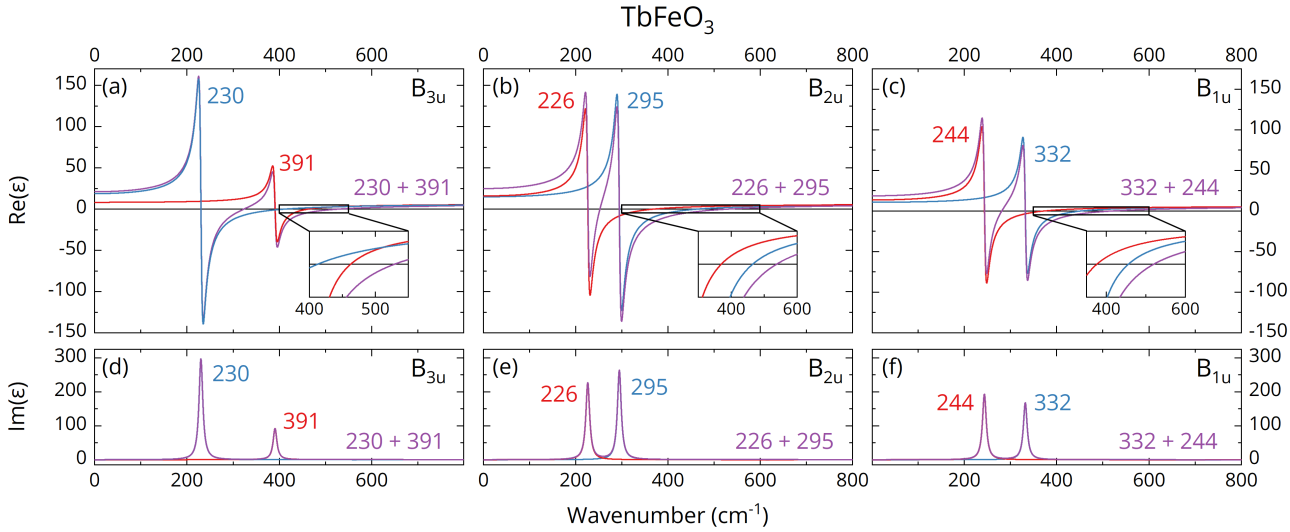

FIG. 6. Calculated spectra of the real and imaginary parts of the dielectric permittivity $\varepsilon(\omega)$ of the (a), (d) B_{3u}, (b), (e) B_{2u} and (c), (f) B_{1u} polar phonons with the highest mode dynamical charges, respectively. The frequencies of the considered polar TO phonon are given.

to the classical Lorentz oscillator model [82; 100]

$$\varepsilon(\omega) = \varepsilon_\infty + \sum_j \frac{S_j}{\omega_{j\mathrm{TO}}^2 - \omega^2 + i\gamma_{j\mathrm{TO}}\omega}, \tag{6}$$

where S_j is the oscillator strength (or mode dynamical charge) of the jth polar TO phonon determined by equation

$$S_{j,\alpha} = \left(\sum_{i,\beta} \frac{1}{\sqrt{M_i}} \xi_{i,j\beta} Z^*_{i,\alpha\beta} \right)^2, \tag{7}$$

where Z^*_i is the Born effective charge of ith atom, respectively and $\xi_{i,j}$ is the ith component of dynamical matrix j^{th} eigenvector, and the other parameters have the same meaning as in Eq. (S1) in SM [62]. It is worth nothing that this classical model [Eq. (6)] can be reduced to the factorized form of the dielectric permittivity [Eq. (S1) in SM [62]] under the assumption of equality of the dampings $\gamma_{j\mathrm{LO}} = \gamma_{j\mathrm{TO}}$. The calculated oscillator strengths S, phonon frequencies ω_{TO} and high frequency dielectric permittivity ε_∞ are listed in Tables VI and III, respectively.

We now consider the model with a single polar mode, which means that the remaining phonon modes of the same symmetry are excluded from the analysis. In this model the eigenvectors of TO and LO modes at the Γ point of the Brillouin zone are identical, $|\xi^{\mathrm{LO}}\rangle = |\xi^{\mathrm{TO}}\rangle$. Then the following relationship for phonon frequencies holds [100; 104]

$$\tilde{\omega}^2_{m\mathrm{LO}} = \omega^2_{m\mathrm{TO}} + \frac{4\pi}{\Omega} \frac{\mathbf{q}\cdot\mathbf{S}_m\cdot\mathbf{q}}{\mathbf{q}\cdot\boldsymbol{\varepsilon}_\infty\cdot\mathbf{q}}\bigg|_{\mathbf{q}\to 0}, \tag{8}$$

where $\tilde{\omega}_{m\mathrm{LO}}$ is the frequency of the LO phonon within single polar mode model. The evaluated $\tilde{\omega}_{m\mathrm{LO}}$ values compared to results of calculations using "real" dynamical matrix with non-analytical term included in Eq. (3) are listed in Table VI. From discrepancy of $\omega_{m\mathrm{LO}}$ and $\tilde{\omega}_{m\mathrm{LO}}$ one readily sees that, in real crystal the LO phonon states correspond to the set of TO polar vibrational modes.

In order to establish the influence of polar TO phonon on LO vibrational states one can simulate the spectrum of $-\Im[\varepsilon^{-1}(\omega)]$, which reveals, as mentioned above, the peculiarities at frequencies of LO phonons. The spectrum is simulated using partial summation in Eq. (6) and plotted in Fig. 7. As an initial approximation, the spectrum was simulated using single polar model (top curves in Fig. 7) by taking into account only TO modes with highest values of oscillator strength S, namely 230 cm^{-1} for B_{3u}, 295 cm^{-1} for B_{2u}, and 332 and 244 cm^{-1} for B_{1u} (Table VI). These modes give the most significant impact among all other modes in spectra $\Im[\varepsilon(\omega)]$ and $-\Im[\varepsilon^{-1}(\omega)]$ (see Fig. 6). Then, by including additional modes in the sum of Eq. (6) the spectrum evolution can by clearly seen as the gradual increasing intensity and frequency of the highest frequency band in the spectra as seen in Fig.7. This effect stems from the fact that individual oscillators modifying the complex dielectric permittivity significantly beyond their resonance TO frequency. Moreover, upon exclusion of TO phonons with the highest oscillator strength, the major high frequency band vanishes as can be seen in Fig. 7 (bottom row). It worth noting that these TO phonons have also the strongest correlation with the highest frequency LO modes (see Fig. 5). Thus, using the highest frequency LO modes as an example, we have demonstrated that the correlation between the LO and TO modes is due to the mixing of harmonic (uncoupled) TO phonons, which reproduces the results obtained using overlap matrix technique shown in Fig. 5.

Obtained results can be summarized as a multimode model with polar modes taking role of dynamical charges with an exciting long range electric field, strength of which is proportional to the dynamical charges of polar phonons. Then the frequency, modulation and strength of the field determine the LO states. This explains the complex nature of LO modes in the real crystals with several polar mode vibrational states. It is interesting to note that, in a similar way, on the example of two harmonic oscillators, it is possible to show a breaking of the "TO-LO" rule. By analyzing the spectrum of the imaginary part of the inverse dielectric permittivity it can be seen that the mode mixing between one phonon with a high mode dynamical charge and a strong LO-TO spitting and another phonon with a small mode dynamical charge and a weak LO-TO splitting inside the first one leads to the frequency inversion $\omega_{\mathrm{LO}} < \omega_{\mathrm{TO}}$ of later phonon [98]. Furthermore, this effect is only caused by the mode mixing because both phonons have dynamic charges of the same sign.

To reveal an unambiguous way in association of the LO modes with the TO ones we performed the lattice dynamical calculations of $TbFeO_3$ with and without the NA term along the high-symmetry path of the Brillouin zone represented in Fig. 9(b). The obtained dispersion curves of phonons are shown in Fig. 8(a). It is clearly seen that taking the NA term into account alters the dispersion curves of some phonons originating from the Γ point of the Brillouin zone only. These dispersion curves at the Γ point correspond to phonons with the symmetry B_{3u}, A_g for Γ–X, B_{2u}, A_g for Γ–Y, and B_{1u}, A_g for Γ–Z paths, as shown in Figs. 8(b)–8(d). Note that, there is an anti-crossings between the modes of the same symmetry, present in both cases, with and without NA term. Furthermore, for most dispersion curves of phonons with the same symmetry the inclusion of the NA term changes the dispersion close to the Γ point, while this effect vanishes at the edge of Brillouin zone because of the long range character of the Coulomb interaction. Thus, analysing these dispersion curves merged at the boundary of the Brillouin zone, one can reliably associate most of the LO and TO modes to each other also at the Γ point. The challenging case arises when dispersion curves (calculated with and without the NA term) that have different symmetries at the Γ point, e.g. B_{3u} and A_g, merge at the

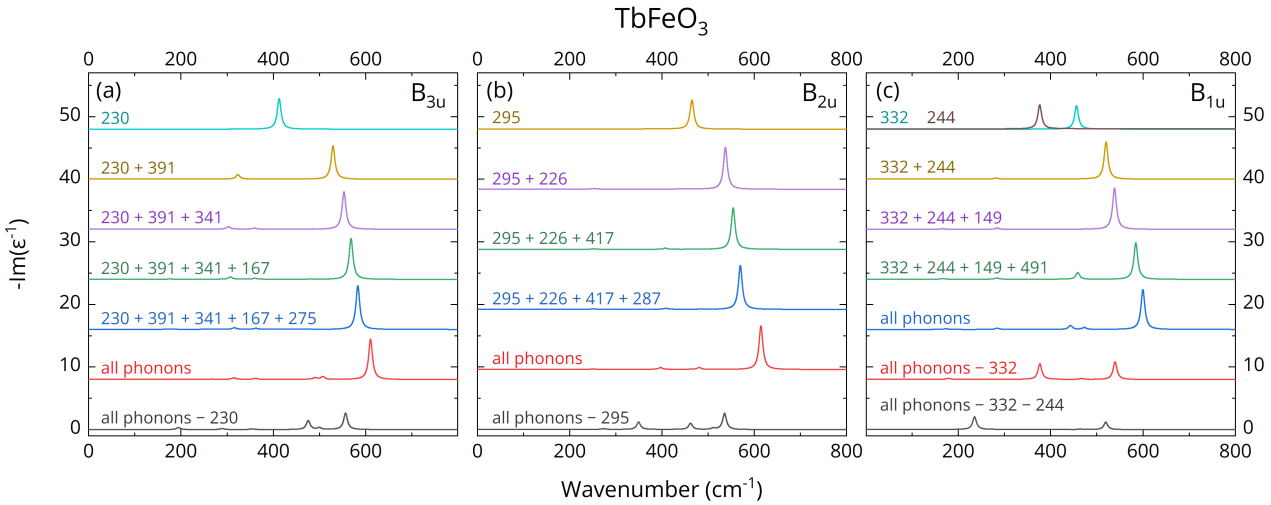

FIG. 7. Spectra of the imaginary part of the inverse dielectric permittivity $-\Im[\varepsilon^{-1}(\omega)]$ with contributions from the (a) B_{3u}, (b) B_{2u}, and (c) B_{1u} polar LO phonons obtained from results of the DFT calculation for orthoferrite $TbFeO_3$ using Eq. (6). The effect of strong mixing of polar TO phonons with high dynamical charges on the highest frequency LO mode which corresponds to the major peak is shown. The frequencies of the considered polar TO phonon are given.

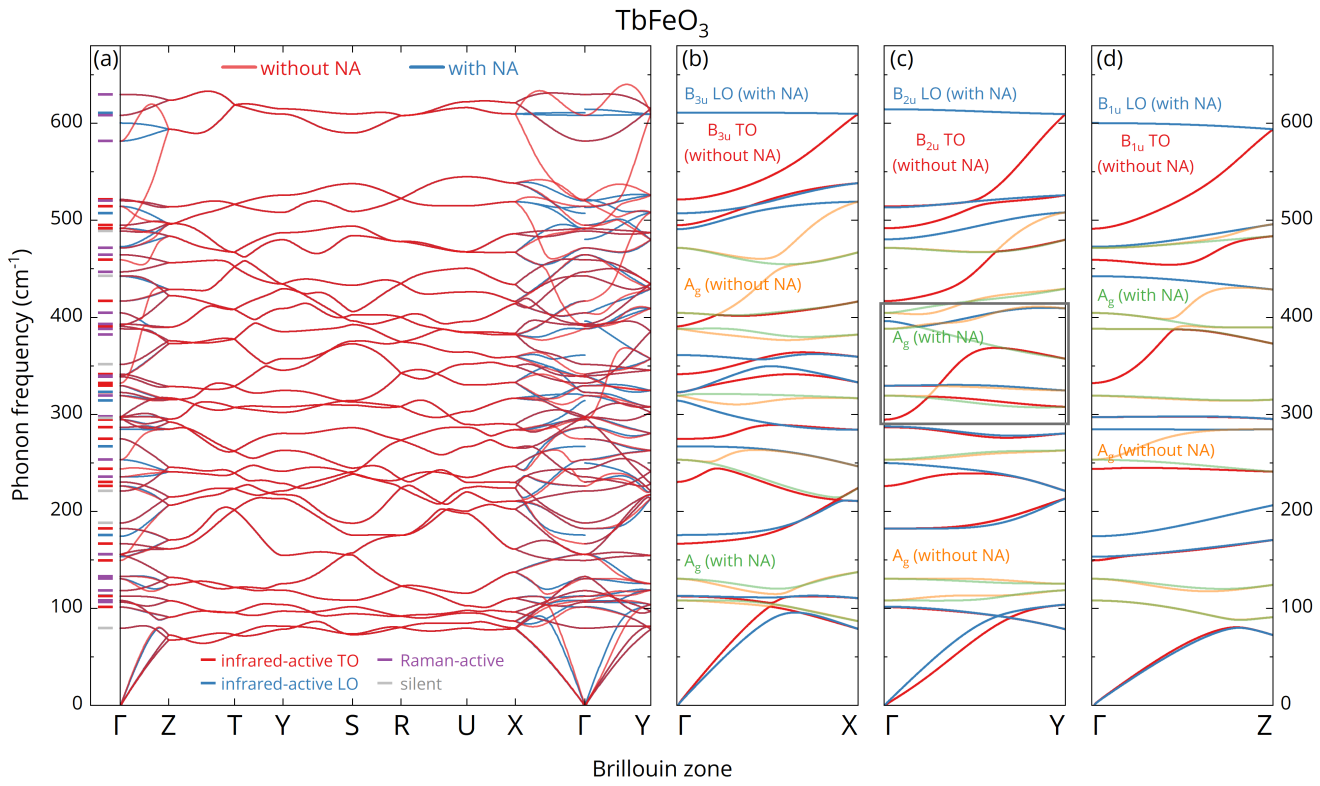

FIG. 8. (a) Full phonon dispersion curves along the Γ–Z–T–Y–S–R–U–X–Γ–Y high-symmetry path of the Brillouin zone for orthoferrite $TbFeO_3$ according to the lattice dynamics calculations with and without the NA term. Dispersion curves for phonons with the same symmetry along the (a) Γ–X, (b) Γ–Y, and (c) Γ–Z paths calculated with and without the NA term. A gray frame marks the conditions for the negative LO-TO splitting. Color bars on the left side of the panel (a) present the calculated phonon frequencies at the Γ point.

boundary of the Brillouin zone.

Through this elaborate analysis of the phonon dispersion curves, it was revealed that, despite the complex form of the correlation matrix C (see Fig. 5), the "LO-TO" rule is not fulfilled for only two polar phonons in $TbFeO_3$. Specifically, the B_{2u} mode with a calculated TO frequency $\omega^S_{\rm TO} = 294.6\,{\rm cm}^{-1}$ has the LO frequency $\omega^S_{\rm LO} = 396.3\,{\rm cm}^{-1}$. This LO mode with strong (S) LO-TO splitting leapfrogs the B_{2u} mode with a frequency $329.6\,{\rm cm}^{-1}$ and very weak (W) LO-TO splitting as shown in Fig. 8(c). In this case, the mode mixing leads to permutation of the TO and LO frequencies and a negative LO-TO splitting $\omega^W_{\rm LO} < \omega^W_{\rm TO}$ occurs according to the theory from Ref. [98]. Moreover, since the phonon dispersion curves of the same symmetry do not cross, the existence of a polar phonon with a negative LO-TO splitting in orthoferrites requires the presence of at least one A_g mode with frequency between $\omega^S_{\rm TO} < \omega_{A_g} < \omega^S_{\rm LO}$ as shown in grey frame in Fig. 8(c). It is worth noting that the negative LO-TO splitting of this phonon is also observed in our experimental results in Fig. 1(b). The assignment of the calculated frequencies of the TO and LO modes allowed us to connect the TO and LO modes obtained in the experiment as listed in Table II. Therefore, the presented analysis of the calculated phonon dispersion curves allowed us to consistently and unambiguously associate TO and LO modes with each other in experimental spectra for $TbFeO_3$.

E. Phonon genesis

In order to complete analysis of the phonon states, we established a genetic relationship between phonons in the orthorhombic and parent cubic phases using group theory. It is known that several paths from parent cubic $Pm\bar{3}m$ to orthorhombic $Pbnm$ phase for perovskites are possible [86; 111]. Among them a sequence of two transformations $Pm\bar{3}m \overset{\rm 1st}{\longleftrightarrow} I4/mcm \overset{\rm 2nd}{\longleftrightarrow} Pbnm$ with the first and second order phase transitions was experimentally confirmed in the perovskite [112]. However, the first order transition considerably obstructs a joint analysis of the lattice dynamics in related phases and revealing the connection between phonons because the lattice parameters and therefore phonon frequencies change abruptly breaking the connection between modes in different phases. On the other hand, the $Pm\bar{3}m \overset{\rm 2nd}{\longleftrightarrow} P4/mbm \overset{\rm 2nd}{\longleftrightarrow} Pbnm$ path is symmetry-allowed and we use this path in our analysis as it allows us to establish a relation between phonons in different phases [86; 113]. It is worth noting that the tetragonal $P4/mbm$ structure is realized in perovskite crystals [114; 115].

The unit cell of $TbFeO_3$ cubic phase ($Pm\bar{3}m$ [#221, O^1_h], $Z = 1$) contains only 5 atoms occupying the Wyckoff positions $1b$ for Tb, $2a$ for Fe, and $3d$ for O as illustrated in Fig. 9(a). The optimized lattice parameter is equal to $a = 3.92$ Å. The group-theoretical analysis of $Pm\bar{3}m$ orthoferrites $RFeO_3$ predicts 5 phonons in the center of the Brillouin zone [86]

$$\Gamma_{\rm total} = \underbrace{T_{1u}}_{\Gamma_{\rm acoustic}} \oplus \underbrace{3T_{1u}}_{\Gamma_{\rm IR}} \oplus \underbrace{T_{2u}}_{\Gamma_{\rm silent}}, \tag{9}$$

The calculation of phonon dispersion reveals a number of imaginary branches, due to the fact that the cubic phase of $TbFeO_3$ is unstable, as shown in Fig. 10(a). The lowest imaginary branch is the one with T_{1u} irreducible representation in the center of the Brillouin zone and M^+_4, R^+_4 and X^+_5 at the M, R, X points of Brillouin zone respectively [see Fig. 9(d)]. The distortions of the structure by displacements of atoms along eigenvectors of the imaginary modes reduce the crystal space symmetry and yield a number of phases with tetragonal and orthorhombic symmetries. The most preferable phase $P4/mbm$ was obtained as a phase with the lowest total energy among all possible structures. The structure was obtained by atomic distortion along the normal coordinate of phonon with M^+_4 irreducible representation at M point of the Brillouin zone. Distortions at the boundary points of the Brillouin zone lead to zone folding, and therefore increasing the volume of the unit cell twice. The transformation matrix of the structural transition P_1:

$$P_1 = \left[\begin{array}{ccc|c} 1 & -1 & 0 & 0 \\ 1 & 1 & 0 & 0 \\ 0 & 0 & 1 & 0 \end{array}\right] \tag{10}$$

where right column denotes the translation vector. The correlation diagram for parent – subgroup irreducible representations is plotted in Fig. 11. It can be clearly seen that the phonon states from the centre of Brillouin zone as well as from the Brillouin zone boundary points X, R, M compose the vibrational states of the tetragonal phase due to Brillouin zone folding.

The optimized lattice parameters of the tetragonal phase of $TbFeO_3$ ($P4/mbm$ [#127, D^5_{4h}], $Z = 2$) are $a = b = 5.49$ Å, and $c = 3.85$ Å, therefore the phase is more compact with respect to the cubic one as shown in Fig. 9(b). The tetragonal unit cell contains 10 atoms occupying the Wyckoff positions $2c$ for Tb, $2a$ for Fe, $2b$ and $4g$ for O. The group-theoretical analysis of $P4/mbm$ orthoferrites $RFeO_3$ predicts 12 non-degenerate and 9 double-degenerate phonons in the center of the Brillouin zone which decompose by irreducible representations according to equation [86]:

$$\Gamma_{\rm total} = \underbrace{E_u \oplus A_{2u}}_{\Gamma_{\rm acoustic}} \oplus \underbrace{A_g \oplus B_{1g} \oplus B_{2g} \oplus E_g}_{\Gamma_{\rm Raman}} \oplus \underbrace{7E_u \oplus 3A_{2u}}_{\Gamma_{\rm IR}} \oplus \underbrace{2A_{1u} + 2B_{1u} + A_{2g}}_{\Gamma_{\rm silent}}, \tag{11}$$

There are several imaginary branches in the calculated phonon dispersion but this number is reduced as compared to the cubic phase as one might expect as shown

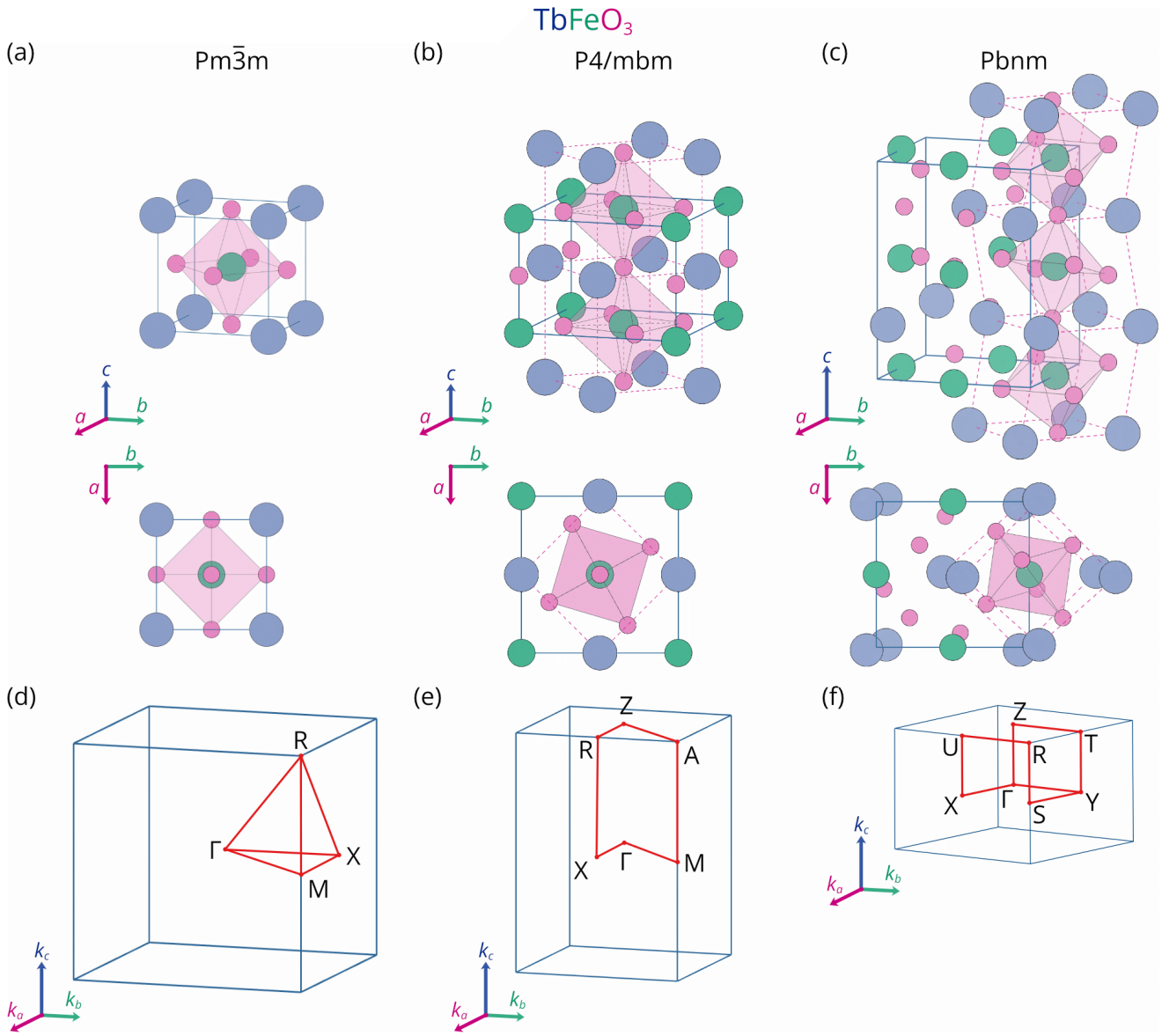

FIG. 9. Crystal structure of the rare-earth orthoferrite $TbFeO_3$ in the (a) cubic $Pm\bar{3}m$, (b) tetragonal $P4/mbm$, and (c) orthorhombic $Pbnm$ phases. Distortions of the ideal cubic perovskite structure are shown by dashed lines. First Brillouin zone of (d) cubic, (e) tetragonal, and (f) orthorhombic lattice indicating high-symmetry points and paths used in the lattice dynamics simulations. The k_a, k_b, and k_c are the primitive reciprocal lattice vectors. Picture was prepared using the VESTA software [110].

in Fig. 10(b). By repeating the stable phase search technique as described above the most stable orthorhombic phase $Pbnm$ is established with the transformation matrix as follows:

$$P_2 = \left[\begin{array}{ccc|c} 1 & 0 & 0 & 0 \\ 0 & 2 & 0 & 0 \\ 0 & 0 & 1 & 1/2 \end{array}\right] \tag{12}$$

The tetragonal to orthorhombic phase transition is induced by condensation of Z_5^+ phonon at the boundary of Brillouin zone (Z point), therefore the structural modification is accompanied by doubling of the unit cell. According to the correlation diagram in Fig. 11 the vibrational states of $TbFeO_3$ in orthorhombic phase are genetically bounded with phonons at the Γ and Z points of Brillouin zone of the tetragonal phase.

The full sequence of structural transformations from the cubic parent phase to orthorhombic one includes doubling of the Brillouin zone twice which leads to a fourfold increasing of a number of vibrational modes. The Brillouin zone zone folding is usually accompanied by the phonon states mixing, and the correlation diagram in the case of $TbFeO_3$ is rather sophisticated due to phonon branches interaction, which reduces the direct connection of vibrational states in parent and orthorhombic phases.

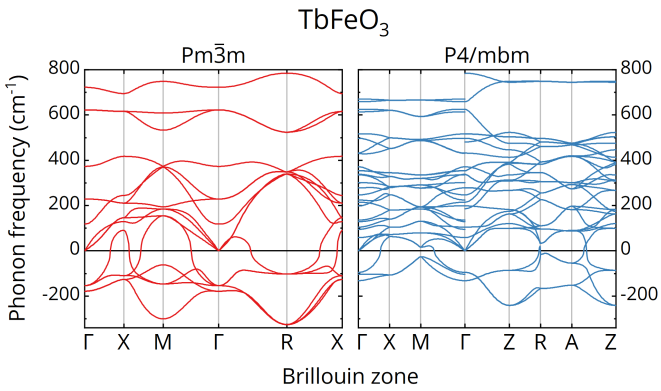

FIG. 10. Full phonon dispersion curves calculated for the (a) cubic $Pm\bar{3}m$ and (b) tetragonal $P4/mbm$ phases of the rare-earth orthoferrite $TbFeO_3$.

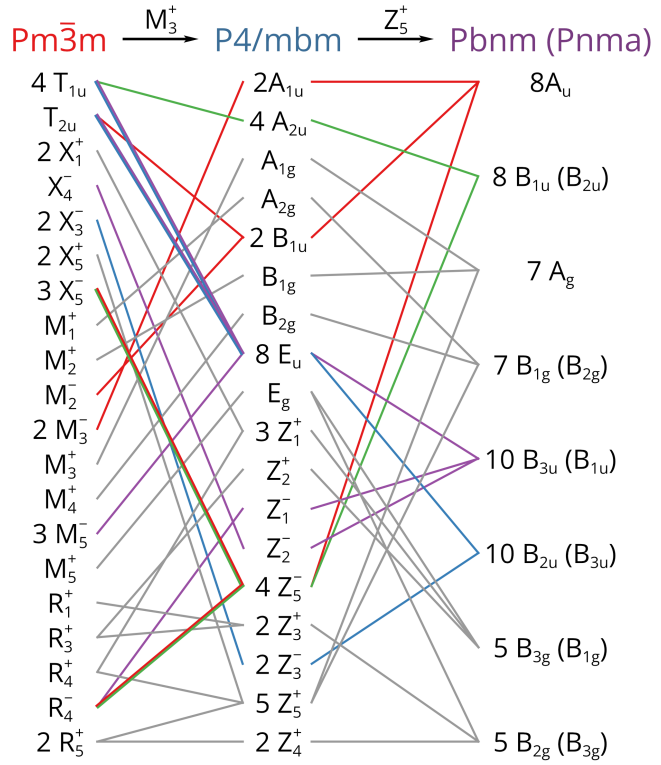

FIG. 11. Correlation diagram between the space group representations for parent cubic $Pm\bar{3}m$ and orthorhombic $Pbnm$ ($Pnma$) phase via intermediate tetragonal $P4/mbm$ one.

The latter explains the multimode influence of TO modes on LO ones as shown in Fig. 5.

III. CONCLUDING REMARKS

In summary, we have studied the polar optical phonons at the center of the Brillouin zone by the polarized infrared reflectivity technique in the rare-earth orthoferrite $TbFeO_3$ single crystal. The spectra of the anisotropic complex dielectric permittivity were extracted from the analysis of the experimental results. The overwhelming majority of predicted TO and LO polar modes were reliably detected according to the polarization selection rules and their parameters were determined. To assign the observed TO and LO modes to each other, we supported the experimental study by the DFT calculation of the lattice dynamics. The obtained frequencies of optical phonons are in fair agreement with the experimental results. We found that according to the correlation analysis between calculated LO and TO mode eigenvectors most LO modes correspond to more than one TO mode in the center of the Brillouin zone due to a strong mode mixing caused by the Coulomb interaction. However, the Coulomb interaction does not affect the phonons at the Brillouin zone boundaries due to its long-range character.

Next, we have analysed the dispersion curves of polar phonons throughout the Brillouin zone calculated both with and without the Coulomb interaction. This allowed us to establish explicit one-to-one relation between LO and TO polar modes at the center of the Brillouin zone despite the complex correlations of their eigenvectors. Furthermore, we found a polar phonon with a negative LO-TO splitting and extended to the Brillouin zone its previously reported general conditions of existence. Additionally, we completed analysis of lattice dynamics in $TbFeO_3$ by measuring angular resolved polarized Raman scattering from Raman-active phonons. Using DFT analysis giving a good agreement with the experimental data, we identify which ionic motions contribute to both infrared- and Raman-active phonons. In particular, we show that Fe^{3+} ion almost do not contribute to Raman-active phonons, which may account for apparent absences of spin-phonon effect on frequencies of these phonons reported in literature. We believe that our results will stimulate further research of the nonlinear phononic and magneto-phononic effects in rare-earth orthoferrites $RFeO_3$ since they explicitly show a degree of mixing between different phonon modes [4; 7; 24–26; 33].

ACKNOWLEDGMENTS

The single crystal grown by A. M. Balbashov was used in the experiments. We thank M. P. Scheglov and N. A. Arkhipov for the help with the x-ray orientation of single crystals. This work was supported by Russian Science Foundation under the grant no. 22-72-00025, https://rscf.ru/en/project/22-72-00025/. A.I.B. acknowledges the support of the Ministry of Science and Higher Education of the Russian Federation (FSWR-2024-0003). N.N.N. and K.N.B. acknowledge a support by the research project FFUU-2022-0003 of the Institute of Spectroscopy of the Russian Academy of Sciences. V.A.C. acknowledges a support by the Ministry of Science and Higher Education of the Russian Federation, project no. FEUZ-2023-0017. R.V.M. acknowledges the support of Royal Society International Exchanges 2021,

grant IES\R2\212182.

[1] R. A. Leenders, D. Afanasiev, A. V. Kimel, and R. V. Mikhaylovskiy, Canted spin order as a platform for ultrafast conversion of magnons, Nature (2024).

[2] A. V. Kimel and A. K. Zvezdin, Universal orthoferrites and orthoferrites as a universe, Photonics Insights **1**, C03 (2023).

[3] X. Li, D. Kim, Y. Liu, and J. Kono, Terahertz spin dynamics in rare-earth orthoferrites, Photonics Insights **1**, R05 (2023).

[4] D. Afanasiev, J. R. Hortensius, B. A. Ivanov, A. Sasani, E. Bousquet, Y. M. Blanter, R. V. Mikhaylovskiy, A. V. Kimel, and A. D. Caviglia, Ultrafast control of magnetic interactions via light-driven phonons, Nat. Mater. **20**, 607 (2021).

[5] X. Li, M. Bamba, N. Yuan, Q. Zhang, Y. Zhao, M. Xiang, K. Xu, Z. Jin, W. Ren, G. Ma, S. Cao, D. Turchinovich, and J. Kono, Observation of Dicke cooperativity in magnetic interactions, Science **361**, 794 (2018).

[6] K. Grishunin, T. Huisman, G. Li, E. Mishina, T. Rasing, A. V. Kimel, K. Zhang, Z. Jin, S. Cao, W. Ren, G.-H. Ma, and R. V. Mikhaylovskiy, Terahertz magnon-polaritons in $TmFeO_3$, ACS Photonics **5**, 1375 (2018).

[7] T. F. Nova, A. Cartella, A. Cantaluppi, M. Först, D. Bossini, R. V. Mikhaylovskiy, A. V. Kimel, R. Merlin, and A. Cavalleri, An effective magnetic field from optically driven phonons, Nature Phys. **13**, 132 (2017).

[8] S. Artyukhin, M. Mostovoy, N. P. Jensen, D. Le, K. Prokes, V. G. De Paula, H. N. Bordallo, A. Maljuk, S. Landsgesell, H. Ryll, B. Klemke, S. Paeckel, K. Kiefer, K. Lefmann, L. T. Kuhn, and D. N. Argyriou, Solitonic lattice and Yukawa forces in the rare-earth orthoferrite $TbFeO_3$, Nat. Mater. **11**, 694 (2012).

[9] S. L. Johnson, Spiers Memorial Lecture: From Optical to THz control of materials, Faraday Discuss. **237**, 9 (2022).

[10] A. V. Kimel, B. A. Ivanov, R. V. Pisarev, P. A. Usachev, A. Kirilyuk, and T. Rasing, Inertia-driven spin switching in antiferromagnets, Nature Phys. **5**, 727 (2009).

[11] A. V. Kimel, A. Kirilyuk, P. A. Usachev, R. V. Pisarev, A. M. Balbashov, and T. Rasing, Ultrafast non-thermal control of magnetization by instantaneous photomagnetic pulses, Nature **435**, 655 (2005).

[12] A. V. Kimel, A. Kirilyuk, A. Tsvetkov, R. V. Pisarev, and T. Rasing, Laser-induced ultrafast spin reorientation in the antiferromagnet $TmFeO_3$, Nature **429**, 850 (2004).

[13] A. Moskvin, Dzyaloshinskii Interaction and Exchange-Relativistic Effects in Orthoferrites, J. Exp. Theor. Phys. **132**, 517 (2021).

[14] A. Moskvin, E. Vasinovich, and A. Shadrin, Simple Realistic Model of Spin Reorientation in 4f-3d Compounds, Magnetochemistry **8**, 45 (2022).

[15] T. Yamaguchi and K. Tsushima, Magnetic Symmetry of Rare-Earth Orthochromites and Orthoferrites, Phys. Rev. B **8**, 5187 (1973).

[16] A. K. Zvezdin and A. A. Mukhin, Magnetoelectric interactions and phase transitions in a new class of multiferroics with improper electric polarization, JETP Lett. **88**, 505 (2008).

[17] Y. Tokunaga, N. Furukawa, H. Sakai, Y. Taguchi, T.-h. Arima, and Y. Tokura, Composite domain walls in a multiferroic perovskite ferrite, Nature Mater. **8**, 558 (2009).

[18] T. N. Stanislavchuk, Y. Wang, S.-W. Cheong, and A. A. Sirenko, Far-IR magnetospectroscopy of magnons and electromagnons in $TbFeO_3$ single crystals at low temperatures, Phys. Rev. B **95**, 054427 (2017).

[19] A. Sasani, J. Íñiguez, and E. Bousquet, Origin of nonlinear magnetoelectric response in rare-earth orthoferrite perovskite oxides, Phys. Rev. B **105**, 064414 (2022).

[20] V. Y. Ivanov, A. M. Kuzmenko, A. Y. Tikhanovskii, A. A. Pronin, and A. A. Mukhin, Observation of Magnetic-Field-Induced Electric Polarization in Terbium Orthoferrite, JEPT Lett. **117**, 38–43 (2023).

[21] E. Hassanpour, Y. Zemp, Y. Tokunaga, Y. Taguchi, Y. Tokura, T. Lottermoser, M. Fiebig, and M. C. Weber, Magnetoelectric transfer of a domain pattern, Science **377**, 1109 (2022).

[22] L. Šmejkal, J. Sinova, and T. Jungwirth, Emerging Research Landscape of Altermagnetism, Phys. Rev. X **12**, 040501 (2022).

[23] K. P. Belov, A. K. Zvezdin, A. M. Kadomtseva, and R. Z. Levitin, Spin-reorientation transitions in rare-earth magnets, Sov. Phys. Uspekhi **19**, 574 (1976).

[24] Z. Zhang, F. Y. Gao, Y.-C. Chien, Z.-J. Liu, J. B. Curtis, E. R. Sung, X. Ma, W. Ren, S. Cao, P. Narang, *et al.*, Terahertz-field-driven magnon upconversion in an antiferromagnet, Nat. Phys. 10.1038/s41567-024-02386-3 (2024).

[25] Z. Zhang, F. Y. Gao, J. B. Curtis, Z.-J. Liu, Y.-C. Chien, A. von Hoegen, M. T. Wong, T. Kurihara, T. Suemoto, P. Narang, *et al.*, Terahertz field-induced nonlinear coupling of two magnon modes in an antiferromagnet, Nat. Phys. 10.1038/s41567-024-02386-3 (2024).

[26] C. Huang, L. Luo, M. Mootz, J. Shang, P. Man, L. Su, I. E. Perakis, Y. X. Yao, A. Wu, and J. Wang, Extreme terahertz magnon multiplication induced by resonant magnetic pulse pairs, Nat. Commun. **15**, 3214 (2024).

[27] J. Han, R. Cheng, L. Liu, H. Ohno, and S. Fukami, Coherent antiferromagnetic spintronics, Nat. Mater. , 1 (2023).

[28] T. Kurihara, M. Bamba, H. Watanabe, M. Nakajima, and T. Suemoto, Observation of terahertz-induced dynamical spin canting in orthoferrite magnon by magnetorefractive probing, Commun. Phys. **6**, 51 (2023).

[29] S. Das, A. Ross, X. Ma, S. Becker, C. Schmitt, F. van Duijn, E. Galindez-Ruales, F. Fuhrmann, M.-A. Syskaki, U. Ebels, *et al.*, Anisotropic long-range spin transport in canted antiferromagnetic orthoferrite $YFeO_3$, Nat. Commun. **13**, 6140 (2022).

[30] A. V. Kimel, A. M. Kalashnikova, A. Pogrebna, and A. K. Zvezdin, Fundamentals and perspectives of ultrafast photoferroic recording, Physics Reports **852**, 1 (2020).

[31] M. T. Dove, *Introduction to Lattice Dynamics*, 4 (Cambridge University Press, 1993).

[32] A. S. Disa, T. F. Nova, and A. Cavalleri, Engineering crystal structures with light, Nat. Phys. **17**, 1087 (2021).

[33] D. M. Juraschek, M. Fechner, and N. A. Spaldin, Ultrafast Structure Switching through Nonlinear Phononics, Phys. Rev. Lett. **118**, 054101 (2017).

[34] H. C. Gupta, M. Kumar Singh, and L. M. Tiwari, Lattice dynamic investigation of Raman and infrared wavenumbers at the zone center of orthorhombic $RFeO_3$ (R = Tb, Dy, Ho, Er, Tm) perovskites, J. Raman Spectrosc. **33**, 67 (2002).

[35] M. K. Singh, H. M. Jang, H. C. Gupta, and R. S. Katiyar, Polarized raman scattering and lattice eigenmodes of antiferromagnetic $NdFeO_3$, J. Raman Spectrosc. **39**, 842 (2008).

[36] Z.-Q. Wang, Y. Mu, Z.-Y. Zeng, X.-R. Chen, and Q.-F. Chen, First-principles study of elastic, dielectric, and vibrational properties of orthoferrites $RFeO_3$ (R = Ho, Er, Tm and Lu), Mater. Res. Express **6**, 055605 (2019).

[37] S. Ahmed, S. S. Nishat, A. Kabir, A. S. H. Faysal, T. Hasan, S. Chakraborty, and I. Ahmed, Structural, elastic, vibrational, electronic and optical properties of $SmFeO_3$ using density functional theory, Phys. B: Condens. Matter **615**, 413061 (2021).

[38] N. Koshizuka and S. Ushioda, Inelastic-light-scattering study of magnon softening in $ErFeO_3$, Phys. Rev. B **22**, 5394 (1980).

[39] S. Venugopalan, M. Dutta, A. K. Ramdas, and J. P. Remeika, Magnetic and vibrational excitations in rare-earth orthoferrites: A Raman scattering study, Phys. Rev. B **31**, 1490 (1985).

[40] M. Mihalik, M. Fitta, M. Vavra, M. Zentková, R. Vilarinho, D. A. Mota, P. Tavares, J. A. Moreira, and A. Almeida, Heat capacity, magnetic and lattice dynamic properties of $TbMn_{1-x}Fe_xO_3$, J. Phys.: Conf. Ser. **592**, 012119 (2015).

[41] M. C. Weber, M. Guennou, H. J. Zhao, J. Íñiguez, R. Vilarinho, A. Almeida, J. A. Moreira, and J. Kreisel, Raman spectroscopy of rare-earth orthoferrites $RFeO_3$ (r = La, Sm, Eu, Gd, Tb, Dy), Phys. Rev. B **94**, 214103 (2016).

[42] A. Panchwanee, V. R. Reddy, A. Gupta, and V. G. Sathe, Study of spin-phonon coupling and magnetic field induced spin reorientation in polycrystalline multiferroic $GdFeO_3$, Mater. Chem. Phys. **196**, 205 (2017).

[43] P. V. Coutinho, F. Cunha, and P. Barrozo, Structural, vibrational and magnetic properties of the orthoferrites $LaFeO_3$ and $YFeO_3$: A comparative study, Solid State Commun. **252**, 59 (2017).

[44] A. Panchwanee, A. Surampalli, and V. R. Reddy, Temperature dependent dielectric and phonon study of polycrystalline $SmFeO_3$, Phys. B: Condens. Matter. **570**, 187 (2019).

[45] J. Saha, Y. M. Jana, G. D. Mukherjee, R. Mondal, S. Kumar, and H. C. Gupta, Structure, möessbauer spectroscopy and vibration phonon spectra in valence-bond force-field model approach for distorted perovskites $AFeO_3$ (A = La, Y), Materials Chemistry and Physics **240**, 122286 (2020).

[46] Y. Ye, A. Cui, M. Bian, K. Jiang, L. Zhu, J. Zhang, L. Shang, Y. Li, Z. Hu, and J. Chu, Temperature and pressure manipulation of magnetic ordering and phonon dynamics with phase transition in multiferroic $GdFeO_3$: Evidence from Raman scattering, Phys. Rev. B **102**, 024103 (2020).

[47] Y. S. Ponosov and D. Y. Novoselov, Lattice and spin excitations of $YFeO_3$: A Raman and density functional theory study, Phys. Rev. B **102**, 054418 (2020).

[48] A. A. Khan, A. Ahlawat, P. Deshmukh, M. Singh, A. Sagdeo, V. Sathe, A. K. Karnal, and S. Satapathy, Magneto-structural correlation across the spin reorientation transition temperature in pure and Sm substituted $TmFeO_3$: A temperature dependent Raman and synchrotron X-ray diffraction study, J. Alloys Compd. **885**, 160985 (2021).

[49] M. C. Weber, M. Guennou, D. M. Evans, C. Toulouse, A. Simonov, Y. Kholina, X. Ma, W. Ren, S. Cao, M. A. Carpenter, B. Dkhil, M. Fiebig, and J. Kreisel, Emerging spin–phonon coupling through cross-talk of two magnetic sublattices, Nat. Commun. **13**, 1 (2022).

[50] B. Mali, J. Sunil, H. S. Nair, C. Narayana, and S. Elizabeth, Spin reorientation to a $\gamma_3(C_x, F_y, A_z)$ configuration and anisotropic spin-phonon coupling in a $Sm_{0.5}Y_{0.5}FeO_3$ single crystal, Phys. Rev. B **105**, 214417 (2022).

[51] P. Eyméoud, C. Turquat, C. Pardanaud, C. Leroux, and A. Merlen, Raman spectroscopic detection of vacancies in $LaFeO_3$, Mater. Lett. **330**, 133296 (2023).

[52] G. V. S. Rao, C. N. R. Rao, and J. R. Ferraro, Infrared and electronic spectra of rare earth perovskites: ortho-chromites,-manganites and -ferrites, Appl. Spectrosc. **24**, 436 (1970).

[53] V. L. Mathe, K. K. Patankar, R. N. Patil, and C. D. Lokhande, Synthesis and dielectric properties of $Bi_{1-x}Nd_xFeO_3$ perovskites, J. Magn. Magn. Mater. **270**, 380 (2004).

[54] M. T. Jamil, J. Ahmad, S. H. Bukhari, and H. Ahmad, Optical phonons and its effect on physical properties of rare-earth orthoferrites $RFeO_3$ (R = La, Nd, Gd, Dy, Er): IR reflectivity measurements, Int. J. Mod. Phys. B **32**, 1850229 (2018).

[55] E. Haye, E. Andre, F. Capon, S. Barrat, M. De La Pierre, R. Dovesi, and C. Carteret, Experimental and theoretical infrared signatures of $REMO_3$ (RE = La, Pr, Nd, Sm, and M = Co, Fe) perovskites, J. Phys. Chem. C. **122**, 10519 (2018).

[56] H. Song and G. Jiang, Effects of Nd, Er doping on the structure and magnetic properties of $YFeO_3$, J. Supercond. Nov. Magn. **31**, 2511 (2018).

[57] L. Suthar, V. K. Jha, F. Bhadala, and M. Roy, Synthesis, electrical and IR spectroscopy of calcium substituted yttrium ferrite ceramics, Mater. Today: Proc. **26**, 3353 (2020).

[58] N. E. Massa, L. del Campo, V. T. Puoc, P. Kaiser, and J. A. Alonso, Low temperature terahertz spectroscopy of $LaFeO_3$, $PrFeO_3$, $ErFeO_3$, and $LuFeO_3$: magnon resonances and ground multiplet transitions, arXiv preprint arXiv:2303.02786 10.48550/arXiv.2303.02786 (2023).

[59] S. Tajima, A. Masaki, S. Uchida, T. Matsuura, K. Fueki, and S. Sugai, Infrared reflectivity and electronic states in perovskite-type oxides $La_{1-x}Sr_xFeO_3$ and $La_{1-x}Sr_xCoO_3$, J. Phys. C: Solid State Phys. **20**, 3469 (1987).

[60] A. D. LaForge, J. Whalen, T. Siegrist, A. P. Ramirez, and Z. Schlesinger, Electron-phonon coupling in $DyFeO_3$ revealed by infrared spectroscopy, arXiv preprint arXiv:1302.2989 (2013).

[61] G. A. Komandin, A. M. Kuzmenko, I. E. Spektor, and A. A. Mukhin, Electric-dipole and magnetic absorption in $TbFeO_3$ single crystals in the THz–IR range, J. Appl. Phys. **133**, 10.1063/5.0149872 (2023).

[62] See Supplemental Material at https://journals.aps.org/supplemental/AAA/BBB for details on the samples of $TbFeO_3$, experimental setups and computational details for studing the lattice dynamics and its analysis. The Supplemental Material contains Refs. [63–88]

[88] A. M. Balbashov, Contemporary Apparatus for Single Crystals Growth of Oxide Compounds and Metals by Optical Floating Zone (FZ), Crystals **9**, 487 (2019).

[64] A. M. Balbashov and S. K. Egorov, Apparatus for growth of single crystals of oxide compounds by floating zone melting with radiation heating, J. Cryst. Growth **52**, 498 (1981).

[65] J. P. Perdew, K. Burke, and M. Ernzerhof, Generalized Gradient Approximation Made Simple, Phys. Rev. Lett. **77**, 3865 (1996).

[66] G. Kresse and J. Furthmüller, Efficiency of ab-initio total energy calculations for metals and semiconductors using a plane-wave basis set, Comput. Mater. Sci. **6**, 15 (1996).

[67] G. Kresse and J. Furthmüller, Efficient iterative schemes for ab initio total-energy calculations using a plane-wave basis set, Phys. Rev. B **54**, 11169 (1996).

[68] S. L. Dudarev, G. A. Botton, S. Y. Savrasov, C. J. Humphreys, and A. P. Sutton, Electron-energy-loss spectra and the structural stability of nickel oxide: An LSDA+U study, Phys. Rev. B **57**, 1505 (1998).

[69] H. J. Monkhorst and J. D. Pack, Special points for Brillouin-zone integrations, Phys. Rev. B **13**, 5188 (1976).

[70] A. Togo and I. Tanaka, First principles phonon calculations in materials science, Scr. Mater. **108**, 1 (2015).

[71] Y. Wang, J. J. Wang, W. Y. Wang, Z. G. Mei, S. L. Shang, L. Q. Chen, and Z. K. Liu, A mixed-space approach to first-principles calculations of phonon frequencies for polar materials, J. Phys. Condens. Matter **22**, 202201 (2010).

[72] L. Maschio, B. Kirtman, R. Orlando, and M. Rèrat, Ab initio analytical infrared intensities for periodic systems through a coupled perturbed Hartree-Fock/Kohn-Sham method, J. Chem. Phys. **137**, 204113 (2012).

[73] L. Maschio, B. Kirtman, M. Rérat, R. Orlando, and R. Dovesi, Ab initio analytical Raman intensities for periodic systems through a coupled perturbed Hartree-Fock/Kohn-Sham method in an atomic orbital basis. I. Theory, J. Chem. Phys. **139**, 164101 (2013).

[74] R. Dovesi, R. Orlando, A. Erba, C. M. Zicovich-Wilson, B. Civalleri, S. Casassa, L. Maschio, M. Ferrabone, M. De La Pierre, P. d'Arco, *et al.*, CRYSTAL14: A program for the *ab initio* investigation of crystalline solids, Int. J. Quantum Chem. **114**, 1287 (2014).

[75] A. D. Becke, Density-functional thermochemistry. III. The role of exact exchange, J. Chem. Phys. **98**, 5648 (1993).

[76] M. Dolg, H. Stoll, A. Savin, and H. Preuss, Energy-adjusted pseudopotentials for the rare earth elements, Theor. Chim. Acta **75**, 173 (1989).

[77] M. Dolg, H. Stoll, and H. Preuss, A combination of quasirelativistic pseudopotential and ligand field calculations for lanthanoid compounds, Theor. Chim. Acta **85**, 441 (1993).

[78] J. Yang and M. Dolg, Valence basis sets for lanthanide 4f-in-core pseudopotentials adapted for crystal orbital ab initio calculations, Theor. Chem. Acc. **113**, 212 (2005).

[79] M. F. Peintinger, D. V. Oliveira, and T. Bredow, Consistent gaussian basis sets of triple-zeta valence with polarization quality for solid-state calculations, J. Comp. Chem. **34**, 451 (2013).

[80] A. B. Kuzmenko, Kramers–Kronig constrained variational analysis of optical spectra, Rev. Sci. Instrum. **76**, 083108 (2005).

[81] M. Schubert, *Infrared Ellipsometry on Semiconductor Layer Structures: Phonons, Plasmons, and Polaritons*, Vol. 209 (Springer Science & Business Media, 2004).

[82] F. Gervais and B. Piriou, Anharmonicity in several-polar-mode crystals: adjusting phonon self-energy of LO and TO modes in Al_2O_3 and TiO_2 to fit infrared reflectivity, J. Phys. C: Solid State Phys. **7**, 2374 (1974).

[83] R. H. Lyddane, R. G. Sachs, and E. Teller, On the Polar Vibrations of Alkali Halides, Phys. Rev. **59**, 673 (1941).

[84] M. Born and E. Wolf, *Principles of Optics: Electromagnetic Theory of Propagation, Interference and Diffraction of Light* (Elsevier, 2013).

[85] L. Martín-Carrón and A. De Andrés, Melting of the cooperative jahn-teller distortion in $LaMnO_3$ single crystal studied by Raman spectroscopy, Eur. Phys. J. B **22**, 11 (2001).

[86] E. Kroumova, M. I. Aroyo, J. M. Perez-Mato, A. Kirov, C. Capillas, S. Ivantchev, and H. Wondratschek, Bilbao crystallographic server: useful databases and tools for phase-transition studies, Phase Transit. **76**, 155 (2003).

[87] R. Loudon, The Raman effect in crystals, Adv. Phys. **50**, 813 (2001).

[88] T. C. Damen, S. P. S. Porto, and B. Tell, Raman Effect in Zinc Oxide, Phys. Rev. **142**, 570 (1966).

[89] M. Eibschütz, Lattice Constants of Orthoferrites, Acta Cryst. **19**, 337 (1965).

[90] M. Marezio, J. Remeika, and P. D. Dernier, The Crystal Chemistry of the Rare Earth Orthoferrites, Acta Cryst. B **26**, 2008 (1970).

[91] A. M. Glazer, The classification of tilted octahedra in perovskites, Acta Crystallogr. B **28**, 3384 (1972).

[92] R. P. Lowndes, Influence of Lattice Anharmonicity on the Longitudinal Optic Modes of Cubic Ionic Solids, Phys. Rev. B **1**, 2754 (1970).

[93] M. Schubert, T. E. Tiwald, and C. M. Herzinger, Infrared dielectric anisotropy and phonon modes of sapphire, Phys. Rev. B **61**, 8187 (2000).

[94] F. Gervais and H. Arend, Long-wavelength phonons in the four phases of $\{N(CH_3)_4\}_2CuCl_4$ and effective charges, Z. Phys. B **50**, 17 (1983).

[95] A. M. Balbashov, G. V. Kozlov, A. A. Mukhin, and A. S. Prokhorov, High frequency processes in magnetic materials (World Scientific Publishing, Singapore, 1995) Chap. Submillimeter spectroscopy of antiferromagnetic dielectrics. Rare-earth orthoferrites.

[96] T. N. Stanislavchuk, Y. Wang, Y. Janssen, G. L. Carr, S.-W. Cheong, and A. A. Sirenko, Magnon and electromagnon excitations in multiferroic $DyFeO_3$, Phys. Rev. B **93**, 094403 (2016).

[97] M. Schubert, A. Mock, R. Korlacki, and V. Darakchieva, Phonon order and reststrahlen bands of polar vibrations in crystals with monoclinic symmetry, Phys. Rev. B **99**, 041201 (2019).

[98] K. D. Fredrickson, C. Lin, S. Zollner, and A. A. Demkov, Theoretical study of negative optical mode splitting in $LaAlO_3$, Phys. Rev. B **93**, 134301 (2016).

[99] M. Wojdyr, Fityk: a general-purpose peak fitting program, J. Appl. Crystallogr. **43**, 1126 (2010).

[100] X. Gonze and C. Lee, Dynamical matrices, born effective charges, dielectric permittivity tensors, and interatomic force constants from density-functional perturbation theory, Phys. Rev. B **55**, 10355 (1997).

[101] W. Zhong, R. D. King-Smith, and D. Vanderbilt, Giant LO-TO Splittings in Perovskite Ferroelectrics, Phys. Rev. Lett. **72**, 3618 (1994).

[102] A. Raeliarijaona and H. Fu, Mode sequence, frequency change of nonsoft phonons, and LO-TO splitting in strained tetragonal $BaTiO_3$, Phys. Rev. B **92**, 094303 (2015).

[103] A. Ratnaparkhe and W. R. L. Lambrecht, Calculated phonon modes, infrared, and Raman spectra in $ZnGeGa_2N_4$, J. Appl. Phys. **128**, 075702 (2020).

[104] C. Lee, P. Ghosez, and X. Gonze, Lattice dynamics and dielectric properties of incipient ferroelectric TiO_2 rutile, Phys. Rev. B **50**, 13379 (1994).

[105] M. Khedidji, D. Amoroso, and H. Djani, Microscopic mechanisms behind hyperferroelectricity, Phys. Rev. B **103**, 014116 (2021).

[106] B. Schrader, *Infrared and Raman spectroscopy: methods and applications* (John Wiley & Sons, 2008).

[107] A. Stupakiewicz, C. S. Davies, K. Szerenos, D. Afanasiev, K. S. Rabinovich, A. V. Boris, A. Caviglia, A. V. Kimel, and A. Kirilyuk, Ultrafast phononic switching of magnetization, Nat. Phys. **17**, 489 (2021).

[108] M. Kwaaitaal, D. G. Lourens, C. S. Davies, and A. Kirilyuk, Epsilon-near-zero regime enables permanent ultrafast all-optical reversal of ferroelectric polarization, Nat. Photon. , 569 (2024).

[109] C. S. Davies and A. Kirilyuk, Epsilon-near-zero regime for ultrafast opto-spintronics, npj Spintronics , 20 (2024).

[110] K. Momma and F. Izumi, *VESTA 3* for three-dimensional visualization of crystal, volumetric and morphology data, J. Appl. Crystallogr. **44**, 1272 (2011).

[111] K. S. Aleksandrov, The sequences of structural phase transitions in perovskites, Ferroelectrics **14**, 801 (1976).

[112] R. Ali and M. Yashima, Space group and crystal structure of the perovskite $CaTiO_3$ from 296 to 1720 K, J. Solid State Chem. **178**, 2867 (2005).

[113] X. Wang, K. Patel, S. Prosandeev, Y. Zhang, C. Zhong, B. Xu, and L. Bellaiche, Finite-temperature dynamics in cesium lead iodide halide perovskite, Adv. Funct. Mater. **31**, 2106264 (2021).

[114] C. D. Martin, S. Chaudhuri, C. P. Grey, and J. B. Parise, Effect of A-site cation radius on ordering of BX_6 octahedra in $(K, Na)MgF_3$ perovskite, Am. Mineral. **90**, 1522 (2005).

[115] D. H. Fabini, C. C. Stoumpos, G. Laurita, A. Kaltzoglou, A. G. Kontos, P. Falaras, M. G. Kanatzidis, and R. Seshadri, Reentrant structural and optical properties and large positive thermal expansion in perovskite formamidinium lead iodide, Angew. Chem. **128**, 15618 (2016).